Role of pre-kinematic fluid-rock interactions on phase mixing, quartz recrystallization and strain localization in low-temperature granitic shear zones

Khadija Alaoui, Laura Airaghi, Benoît Dubacq, Claudio L Rosenberg, Nicolas Bellahsen, Jacques Précigout

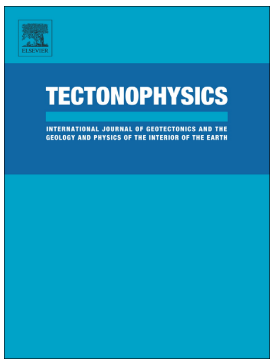

Role of pre-kinematic fluid-rock interactions on phase mixing, quartz recrystallization and strain localization in low-temperature granitic shear zones

Khadija Alaoui, Laura Airaghi, Benoît Dubacq, Claudio L. Rosenberg, Nicolas Bellahsen, Jacques Précigout

PII: S0040-1951(23)00033-1

DOI: https://doi.org/10.1016/j.tecto.2023.229735

Reference: TECTO 229735

To appear in: *Tectonophysics*

Received date: 30 July 2022

Revised date: 23 January 2023

Accepted date: 25 January 2023

Please cite this article as: K. Alaoui, L. Airaghi, B. Dubacq, et al., Role of pre-kinematic fluid-rock interactions on phase mixing, quartz recrystallization and strain localization in low-temperature granitic shear zones, *Tectonophysics* (2023), https://doi.org/10.1016/j.tecto.2023.229735

Role of pre-kinematic fluid-rock interactions on phase mixing, quartz recrystallization and strain localization in low-temperature granitic shear zones

Khadija Alaoui[1,2], Laura Airaghi[1,2], Benoît Dubacq[2], Claudio L. Rosenberg[2], Nicolas Bellahsen[2] and Jacques Précigout[1]

[1]Institut des Sciences de la Terre d'Orléans (ISTO), UMR 7327, CNRS-BRGM, Université d'Orléans, 45071, Orléans, France

[2]Institut des Sciences de la Terre de Paris (ISTEP), UMR 7193, CNRS-INSU, Sorbonne Université, 75005, Paris, France

Corresponding author: laura.airaghi@univ-orleans.fr

ORCID ID Khadija Alaoui: https://orcid.org/0000-0001-6991-6355

Abstract

This study explores the relative importance of fluid availability, temperature and mineral assemblage variations on the development of macro and microstructures in greenschist-facies shear zones of two granitoids of the Axial Zone (central Pyrenees) emplaced at the end of Variscan orogeny, at similar structural levels. The investigated shear zones formed during alpine compression at comparable temperature. In the Bielsa granitoid, deformation was distributed in a dense network of shear zones. Extensive mineralogical transformations resulted in variations in major, minor and rare earth element contents pointing to pre-kinematic hydrothermal alteration (at Permian-Triassic) at 270-350°C and further alteration in fluid-abundant conditions during Alpine shearing. Quartz was fractured, exhibits weak plastic deformation and was weakly reworked, mainly by dissolution-reprecipitation. Strain was accommodated in the mica-rich matrix (40-50 % vol. of mica). Mica significantly grew during pre-kinematic hydrothermal alteration. In the Maladeta granite, deformation was localized in sparse shear zones. Hydrothermal alteration occurred at similar to slightly higher temperature (280-380°C). Elemental variation related to alteration was weaker, pointing to fluid-deficient conditions before and during Alpine compression. Limited fluid resulted in lower mica content (20-28 % vol.) than in Bielsa. Quartz exhibits stronger intragrain plastic deformation, dynamic recrystallization by subgrain rotation and reworking by dissolution-reprecipitation and nucleation. Strain was accommodated by both quartz aggregates and mica-rich matrix. The transition from dominant brittle behavior of quartz to dynamic recrystallization by subgrain rotation occurred in a narrow range of 350-380°C, well below 450°C as generally described. The lower temperature and less hydrated conditions in Maladeta are in apparent contradiction with stronger quartz recrystallization and strain localization than in Bielsa. By promoting phyllosilicate growth and phase mixing before shearing, the metamorphic pre-conditioning of the granitic protolith appears to be the main factor controlling strain distribution at sample scales and differences in tectonic styles between the two massifs.

Key words: Greenschist-facies shear zone – Mass transfer – Quartz deformation – Bielsa and Maladeta granitoids – Axial zone of Pyrenees

1. Introduction

Differences in mechanisms of strain accommodation are often observed in crustal shear zones of granitic composition formed at different depths. The rheological behavior of feldspars and quartz - the major components of granitic rocks - strongly controls the overall rock strength and varies with syn-tectonic temperature, fluid availability and variations of differential stress and/or strain rate (e.g. Stipp et al., 2002; Piazolo et al., 2002 and references therein). It was shown that, for example at greenschist-facies conditions, deformation of quartz in metapelites may shift from brittle to plastic within ~ 50°C (T ~ 250-300°C, Stöckhert et al., 1999) and its dynamic recrystallization regime may change from bulging (regime I) at T < 450°C to subgrain rotation (regime II) at 450°C < T < 500°C (at constant strain rate, Stipp et al., 2002). However, what is more difficult to explain is that different microstructures and microtextures of quartz can be observed in shear zones that formed at very similar crustal depths, as in the case of brittle-plastic transition under greenschist-facies conditions (e.g. Spruzeniece and Piazolo, 2015). At these conditions, fluid availability, which is well documented in shear zones (O'Hara, 1988; Rolland et al., 2003) promotes quartz recrystallization (e.g. Spruzeniece and Piazolo, 2015, Palazzin et al., 2018) and favors textural re-organization at the macro- and micro-metric scale as well as mineral reactions (e.g., McCaig et al., 1984; Fitz Gerald and Stünitz 1993; Wintsch et al., 1995; Wibberley, 1999; Goncalves et al, 2016). Mineral reactions often result in phase mixing that may cause rock weakening by preventing grain growth due to pinning of grain boundaries (e.g., Etheridge and Wilkie, 1979; Herwegh et al., 2011). Specifically, the growth of phyllosilicates also lowers the overall rock strength (e.g. Gueydan et al., 2003), and inhibits recrystallization and development of crystal preferred orientation (CPO) of quartz (Song and Ree, 2007; Hunter et al., 2016). At larger scale, phyllosilicate abundance controls the structural style (location of shear zones) and the strain intensity of the bulk rock (Wehrens et al., 2016; Airaghi et al., 2020a; Graziani et al., 2020).

The timing of phyllosilicate growth in deformed granite strongly relates to (i) fluid influx, (ii) the mechanisms of fluid percolation and (iii) the composition of the fluid phase (Rossi et al., 2005; Cenki-Tok et al., 2014; Rossi and Rolland, 2014). While some greenschist-facies shear zones are almost iso-chemical and evolve as closed system (Kerrich et al. 1980; Hippertt, 1998), others show open-system

behavior with significant mass transfer, either at an early stage of the shear zone development (Rolland et al., 2016, Tursi et al. 2021), or at a later stage (i.e. Glanzner and Bertley, 1991; Rolland and Rossi, 2016; Tursi et al., 2018; Ceccato et al., 2022). As a consequence, no systematic timing of phyllosilicate growth and phase mixing in the development of shear zones can be assessed. Their relative importance over microstructural development and mechanisms of strain accommodation remain therefore difficult to compare to the effect of varying temperature.

The present work investigates structural and microstructural differences in shear zones of two Variscan granitoids of the central Pyrenees (Bielsa and Maladeta). Located at ~ 40 km from each other, the two granitoids are altered in greenschist-facies conditions. Both granitoids were deformed during Alpine orogeny (Airaghi et al., 2020a, Bellahsen et al., 2019 and references therein). Two different alteration events were recognized in the Bielsa granitoid: the first during Permian-Triassic time, at the end of Variscan orogeny (230-300 Ma), the second during Alpine compressional stage (40-70 Ma, Airaghi et al., 2020a). Microstructures, mineral abundance, whole-rock chemistry, syn-kinematic temperature conditions and quartz deformation mechanisms across shear zones of the two massifs have been studied and compared. Our results highlight the key role of pre-kinematic (pre-Alpine shearing) alteration on strain localization, leading to drastically different responses to deformation at similar temperatures.

2. Geological setting

The Axial Zone of the central Pyrenees (Fig. 1a) consists of a series of basement slices forming a South-verging fold-and-thrust system (Fig. 1b-c, Roure et al., 1989; Munoz., 1992). The basement of the Axial zone is mainly composed of granitic plutons (e.g., Maladeta, Bielsa, Néouvielle and Eaux-Chaudes) emplaced during Variscan orogeny (*c.* 300 Ma, Román-Berdiel et al., 2004). Alpine shortening was accommodated on thrusts active from 70 Ma to Oligocene times (Wayne and McCaig, 1998; Roman-Berdiel et al., 2004; Jolivet et al., 2007; Abd Elmola et al., 2018; Bellashen et al., 2019; Airaghi et al.,

2020a). Metric to decametric-scale shear zones in granitic plutons formed during the alpine shortening (e.g. Ingles et al., 1999).

The Bielsa granitoid forms the largest part of the Bielsa thrust sheet delimited to the North by the South-verging Millares and the Gavarnie thrusts and to the South by the Guarga thrust (Fig. 1b, Casas et al., 2003; Roman-Berdiel et al., 2004). Triassic sediments unconformably overly the crystalline massif, suggesting a shallow structural position of Bielsa during Permian time (Fig. 1d). Shortening is distributed within the massif (Fig. 1b), as shown by anastomosed nets of closely-spaced (~ 100-200 m) shear zones in the area of lake Urdiceto (Fig. 1d) and by the folded interface between the crystalline basement and its sedimentary cover (Bellahsen et al., 2019). The massif experienced fluid-rock interactions in the time range of Permian-Early Triassic (230 300 Ma, i.e. at least 150-200 Ma before Alpine shortening), at 300-350°C (Airaghi et al., 2020a). Shear zone formation during Alpine compression was also accompanied by fluid-rock interactions (*c*. 40-70 Ma, Airaghi et al. 2020a) at ~ lower temperature conditions of 250-280°C. This is consistent with zircon fission track (ZFT) ages showing that the Bielsa granitoid experienced T < 350°C since the Mesozoic (143-161 Ma, Bellahsen et al., 2019).

The Maladeta granitoid is part of a complex of several plutons (Michard-Vitrac et al., 1980) exposed over ~450 km² (Fig. 1a) and emplaced into Cambrian to Carboniferous metasediments during the Late Carboniferous (Metcalf et al., 2009). $^{40}Ar/^{39}Ar$ dating on K-feldspar suggests burial of the massif during Alpine shortening by the activation of the Gavarnie thrust (Fig. 1c), then exhumed at *c*. 50 Ma (Metcalf et al., 2009). Both Mesozoic and Cenozoic ZFT ages (Sinclair et al., 2005; Waldner et al., 2021) suggest that the massif resided in the high range of temperature traditionally assumed for partial retention zone of ZFT (280 ± 50 °C) until 30-35 Ma. As for the Bielsa granitoid, Maladeta was in a shallow structural position during Permian time (even if probably slightly deeper than Bielsa). This is suggested by an unconformity between the granite and Triassic sediments cropping out in the northern edge of the massif, but not within the massif itself (Fig. 1e, Metcalf et al., 2009, and references therein). However, in contrast to Bielsa, only few shear zones (~50 m wide) have been found in the Maladeta

granite (Fig. 1e, Bellahsen et al., 2019), separated by ~1.5 km large portions of undeformed granite (Fig. 1e; Bellahsen et al. 2019, Waldner et al., 2021).

3. Sampling

In Bielsa, seventeen samples were collected east of the Urdiceto lake (Fig. 1d), across two brittle-ductile crustal shear zones, along N-S oriented transects of 10 to 15 m long, at the boundary with the Triassic sediments (transect B1 of Fig. 2a and transect B2 of Fig. 2b). Transect B1 (samples from ZAL18-14A to ZAL18-14I) includes undeformed granitoid in the southern part and a mylonitic corridor of c. 5 m width in the central part (Fig. 2a and 3a-c). In transect B2 (samples from ZAL18-17A to ZAL18-17H), the transition from the least deformed granitoid to high strain rocks takes place within ~ 3 m (Fig. 2b and 3d-f).

In Maladeta, samples were collected along a 30 m long transect across one of the rare shear zones of the massif (Fig. 2c), next to lake Estany de Cavallers (Fig. 1e). Seven samples (ZAL18-19A to ZAL18-19C, ZAL18-20C to ZAL18-20E, ZAL18-22) were selected for this study. The samples are representative of the variations in strain and mineralogy. Although the strain gradient is more discontinuous in this transect than across Bielsa shear zones, a progressive textural and structural evolution is observed from undeformed granite (ZAL18-22) to highly strained samples (ZAL18-20E), with increasing abundance of white mica and chlorite, and decreasing grain size (Fig. 3g-i).

4. Methods

Mineral abundance was estimated by identifying mineral phases in > 500 points on thin-section scans with the software JMicroVision v1.2.7 (https://www.jmicrovision.com). Backscattered electron images have been acquired using a scanning electron microscope (SEM) Zeiss Supra 55VP at ISTeP (Sorbonne Université, Paris). Quartz deformation textures were investigated by electron backscatter diffraction (EBSD) using an EDAX PEGASUS system (OIM DC 6.4 software) connected to a TESCAN SEM

(MIRA3) located at the *Bureau de Recherches Géologiques et Minières* (BRGM, Orléans). Analytical conditions were: 20 kV of accelerating voltage, a working distance of 15 or 18 mm, a probe current of 6 nA, and a step-size of 1 μm. Data were reduced using the OIM analysis 7.0 software by applying the "cleaning" procedure described by Précigout et al. (2017; 2019), and then processed with the open-source MTEX toolbox for MATLAB (http://mtex-toolbox.github.io/). The texture (*J*; Bunge, 1982) and misorientation (*M*; Skemer et al., 2005) indices have been calculated to quantify the fabric strength for each map. Kernel average misorientation (KAM, Kilian and Heilbronner, 2017) maps were also calculated from the average misorientation angle of a given pixel with respect to its closest neighbors and considering two rows of neighboring pixels (order = 2) with a threshold angle of 10°. The KAM maps required to denoise the EBSD maps using a half quadratic filter (see the MTEX website: *mtex-toolbox.github.io*). The gKAM (mean KAM of a given grain) then provided a proxy for the intragranular deformation intensity (Kilian and Heilbronner, 2017).

Quantitative point analyses of chlorite and white mica were acquired with a CAMECA SX-Five electron probe micro-analyser (EPMA) at CAMPARIS (Sorbonne Université, Paris, France). Analyses have been performed at 15 kV and 10 nA with a ~ 1 μm beam size in wavelength dispersive spectroscopy (WDS) mode and using diopside (Ca, Mg, Si), $MnTiO_3$ (Mn, Ti), orthoclase (K, Al), hematite (Fe), albite (Na), and Cr_2O_3 (Cr) as standards for measuring the elements written in brackets. EPMA data were quantified with the PAP procedure (Pouchou et al., 1991).

Whole-rock composition was obtained for major elements by inductively-coupled plasma optical emission spectrometry (ICP-OES), after grounding and acid attack of the rock samples. The instrument used was an Agilent 5100 of the ALIPP6 facility at ISTeP (Sorbonne Université, Paris). Trace and rare earth elements (REE) were measured by inductively coupled plasma mass spectrometry (ICP-MS), using an Agilent 8800 instrument at ALIPP6. Standards used were: RGM-1 (rhyolite), BIR-1 (basalt), AGV-2 (andesite), LIP (rhyolite), HAM (rhyolite), M77-2 (rhyolite), GSN (granite), CO5 (rhyolite), BHVO-2 (basalt), MAN (granite), JB-1 (basalt) and JR-1 (rhyolite). Volatile concentrations were measured by loss on ignition (LOI).

The range of crystallization temperature of chlorite was estimated, from chlorite chemical composition obtained with EPMA (Table S1), using the semi-empirical thermometer of Bourdelle et al.

(2013) in its graphical form (Bourdelle and Cathelineau, 2015). The Chl-Qz-H_2O multi-equilibria thermodynamic model of Vidal et al. (2006) was also used for comparison at a reference pressure of 3 kbar and water activity of unit value. The absolute uncertainty on the crystallization temperature estimates is ~ 50°C (Vidal et al., 2006).

5. Petrography and microstructures

Petrographic observations are presented from the less to the most altered and deformed sample of each transect (Fig. 3), where the degree of alteration and deformation is qualitatively estimated from the development of cleavage, grain size reduction, phyllosilicate abundance and interconnectivity. For the Bielsa granitoid, detailed petrographic and mineralogical descriptions of complementary samples can be found in Airaghi et al. (2020b); only the main petrographic features are presented below for this granitoid, completed by grain size and mineral proportions. Chemical compositions of chlorite and white mica are presented in Table S2.

5.1 Bielsa granitoid

In samples of Bielsa, the undeformed granitoid exhibits a magmatic texture (Fig. 3a) but it is altered under greenschist-facies conditions during the Permian-Triassic hydrothermal event (Airaghi et al., 2020a, b). Rock re-equilibration under greenschist-facies conditions progressively increases with increasing strain (Fig. 3a-f, 4a-c).

5.1.1 Bielsa B1 transect

In undeformed samples of transect B1, the relict magmatic mineral assemblage is made of K-feldspar, plagioclase, quartz, biotite and amphibole (ilmenite and zircon as accessory phase, Fig. 3a, 4a). Biotite and amphibole (from less than 1 mm to 4 mm in size) are altered to chlorite ± white mica grains of 500 µm in size (± titanite or anatase, ± prehnite, ± quartz, Fig. 4a and Fig. S1a). Feldspar grains (~ 2-3 mm)

show extensive sericitization with heterogeneous aggregates made of relict K-feldspar, albite, white mica and quartz grains of a few microns to 50 µm in size (Fig. 4a, 5a-e). Larger quartz grains have an average size of 2.5 mm with no or little undulose extinction and abundant fluid inclusions (Fig. 4d, e).

Medium to high strain samples (e.g. ZAL18-14E, ZAL18-14B) show a fabric made of mica and quartz porphyroclasts (Fig. 3b, c and 4b, c). Chloritization of biotite and sericitization of feldspar is almost complete (Fig. 4b, c). Quartz grains are mainly fractured perpendicular to foliation but show little dislocation (Fig. 3c, 4c). Fractures are filled with white mica or calcite (Fig. 4c, f). Larger quartz grains are richer in fluid inclusions than in undeformed samples (Fig. 4c, e and f). They exhibit undulose extinction, narrow, planar deformation bands (white dashed line marked as NDF in Fig. 4e) and wider (20 µm) deformation bands with different orientation and extinction angles with respect to the surrounding grain (WDF, white arrows in Fig. 4f). Incipient dynamic recrystallization by bulging is observed very locally (BLG in Fig. 4e). Fine-grained quartz (20-30 µm, Fig. 4c) is dispersed in the mica matrix (Fig. 4c, f). White mica shows a strong shape preferred orientation parallel to the foliation in all high strain samples (Figs 3c and 4c). K-feldspar relicts deform in a brittle way. Calcite is observed in the matrix and within cracks of quartz fragments (Fig. 4b-c). Calcite in the matrix is plastically deformed (Fig. S1b).

In terms of mineral proportions, from undeformed granitoid to mylonite, the abundance of quartz remains overall constant (Fig. 6a), the proportion of feldspar strongly decreases and the one of white mica increases. This results in a mica-quartz ratio varying from ~0.9 to ~1.2. Calcite proportions increase from 1 % vol. (undeformed granite) to 8 % vol. in high strain samples (Fig. 6a).

5.1.2 Bielsa B2 transect

Samples from transect B2 share similar characteristics with samples of transect B1, for equivalent degree of deformation (e.g., Fig. 3d-f and 7a-f), except that:

(i) the overall grain size is smaller than in the high strain samples of B1 (i.e. ~ 10 µm for white mica, ~ 100 µm for quartz, Fig. 7c, f, Table 1);

(ii) large quartz grains (5 to 1 mm) exhibit some intragrain deformation also in the less deformed samples, as lenticular NDB subparallel to fluid inclusions planes (Fig. 7d, e) cross-cut by WDB parallel to the c axis of the host grain (WDB in Fig. 7d, e).

(iii) in high strain samples, patchy patterns of domains with different orientations are observed (white arrows in Fig. 7f) along with straight alignements of misoriented quartz grains (yellow arrows in Fig. 7f). Larger quartz grains also show a spongy texture, due to abundant fluid inclusions (Fig. 7f). Around larger quartz grains, aggregates of very fine-grained quartz (1-5 µm, Fig. 7f) and matrix minerals are observed, separated by lobate and 'diffuse' boundaries (Fig. 7f).

(iv) the proportion of fine-grained quartz dispersed in the matrix mica relative to large quartz grains is higher (Fig. 3f, 7c);

(v) the proportion of white mica increases more abruptly with increasing strain (Fig. 6b), resulting in higher mica-quartz ratio (1.8) in high strain samples than in B1 transect;

5.2 Maladeta granitoid

In the Maladeta granitoid, the undeformed samples exhibit a magmatic texture (Fig. 3g) and the magmatic mineral assemblage is largely preserved (Fig. 3g and Fig. 8a) The pristine assemblage consists in K-feldspar, plagioclase, quartz, white mica and biotite as major phases. The mica-quartz ratio across the Maladeta transect varies only slightly with increasing strain (from 0.5 to 0.8) and modal abundances remain rather constant (Fig. 6c).

In the undeformed sample (ZAL18-22), white mica constitutes ~ 20 % vol. of the mineral assemblage (with a few % of it of magmatic origin). Quartz is millimeter-sized (~ 3-5 mm) in the undeformed granite, and it is characterized by incipient undulose extinction (Fig. 8a, d).

In medium and high strain samples (e.g. ZAL18-20D and ZAL18-20E, Fig. 3h and i), relicts of magmatic K-feldspar are largely preserved (Fig. 8b-c) along with aggregates of quartz (parent and secondary grains). They alternate with mixed layers of variable width (10 to 500 µm) made of

phyllosilicates (fine-grained white mica of 10-100 μm and chlorite grains of 100-500 μm) and quartz, overall defining the mylonitic foliation plane (Fig. 3i, 8c). In quartz-rich aggregates, large quartz grains show deformation bands (yellow arrows in Fig. 8e), with few new grains within these bands, or local pockets of new grains. New quartz grains highly misoriented relative to parent grains fill the intra-grain microcracks (white arrows in Fig. 8e). Microcracks coalesce in conjugate fractures, or evolve into shear bands (Fig. 8e). Larger quartz grains (white arrow in Fig. 8f) are subdivided in progressively misoriented subgrains and mantled by polygonal subgrains (~ 10 μm, yellow arrows in Fig. 8f) to form core-mantle structures. Bulging is only locally observed.

6. Electron backscatter diffraction of quartz

Intragranular misorientations, kernel average misorientation, grain size and CPO have been quantified for quartz using EBSD in high strain samples (Bielsa B1: ZAL18-14B; Bielsa B2: ZAL18-17C; Maladeta: ZAL18-20E) and in two medium strain samples (Bielsa: ZAL18-17B and Maladeta: ZAL18-20C). CPO are constructed using one-point-per-grain in equal-area lower-hemisphere pole figures (Figs. 9-11). Quartz-rich areas were selected for EBSD analyses to be representative of quartz deformation and recrystallization of the samples. Grains are defined as areas delimited by high-angle (≥ 10°) boundaries (Halfpenny et al., 2012) and a minimum of 5 indexed consecutive pixels on several rows. Low-angle boundaries are identified as segments within the grains showing a misorientation angle ≥ 2° between two pixels (Trimby et al., 1998). Recrystallized quartz grains were distinguished from parent grains on the basis of their size (Bielsa) or orientation spread (GOS), following the procedure proposed by Cross et al. (2017). Table 1 summarizes the characteristics of parent and recrystallized quartz grains.

6.1 Recrystallization of quartz in Bielsa shear zones

In Bielsa samples, two populations of quartz are recognized from grain size (Table 1). Larger quartz grains (Qz1) have a grain size larger than 50 μm (Figs. 9 a-b, 10a-b and Table 1) and show higher aspect ratio than smaller grains (Qz2), although the overall aspect ratio remains low (< 3, Table 1). Intra-grain misorientation angles of 2° to 50° are observed in Qz1 (Table 1), along lenticular planar deformation

bands (white arrows in Fig. 9b, 10b) and in perpendicular wider deformation bands (yellow arrows in Fig. 9b) as the NDB and WDB observed in figure 7e. In the more deformed transect B2, Qz1 shows elongate patchy domains with orientation misfits (Fig. S3b). No polygonal subgrains are observed in Qz1 (Figs. 9b, 10b and Fig. S3b). Grains of Qz2 mainly form isolated grains randomly distributed within mixed white mica-quartz layers (Fig. 9b, 10b). They show barely intra-grain misorientation (misorientation angles close to 0°, Fig. 9b, 10b, Fig. S2b). In phyllosilicate-rich areas (Fig. S3a-b), quartz exhibits a smaller average grain size (5-12 µm; Table 1) than in quartz-rich areas.

Mean grain-KAM values (gKAM) for Bielsa are comprised between 0.59 and 1.02 (Table 1, Fig. 9d, 10d, S2d, S3d) and a few, small grains of quartz are included in Qz1 porphyroclasts in zones of high grain misorientation (yellow arrows in Fig. 10d and S2d). The quartz CPO is weak (Fig. 9c, 10c, S2c, S3c, Table 1), and there is no clear CPO for sample MAL 18-14B (Fig. 9c). Different slip systems operate in quartz of these samples (prism <a> in Fig. 9c, 10c, S2c and rhomb <a> in Fig. S3c) with no predominance of one system over the other.

6.2 Recrystallization of quartz in the Maladeta shear zone

In Maladeta samples, where microstructures suggest that dynamic recrystallization may occur (Fig. 11a), the GOS criterion of Cross et al. (2017) was used to separate parent (Qz1) and dynamically recrystallized (Qz2) grains (Table 1). Parent Qz1 show intra-grain misorientation angles up to 40° and exhibit polygonal subgrains of similar shape and size than recrystallized ones (Fig. 11b, S4b). Polygonal subgrains are also aligned along one or more families of planes (Fig. 11b). Small Qz2 grains are more abundant than in Bielsa samples. They mantle Qz1 or cluster in quartz-rich layers parallel to the foliation (Fig. 11a, b and d, Fig. S4 a-b). The size and amount of Qz1 progressively decreases while the abundance of Qz2 increases from medium to high strain samples (Table 1).

Mean gKAM values are lower than in Bielsa (0.29-0.35; Table 1, Fig. 11d, S4d). Micrometric polygonal Qz2 grains are locally arranged in arrays cross-cutting Qz1 porphyroclasts (Fig. 11b, d and S4b, d). They are located along intra-grain boundaries and in areas with elevated KAM values corresponding to subgrain boundaries, areas of accumulation of dislocations (yellow arrows in Fig. 11d

and S4d). The low *J* and *M* indices (similar to those in Bielsa, Table 1, Fig. 11c and S4c) indicate weak fabric despite extensive quartz reworking. Similarly, to Bielsa, the distribution of quartz misorientation axes across low-angle boundaries shows multiple slip systems, i.e., rhomb <a>, basal <a> (Fig. 11c) and prism <a> (Fig. S4c) with no obvious predominance of one over the other. None of the identified quartz slip-systems neither fully coincide with the CPO fabric nor the kinematic framework.

7. Whole-rock chemistry

Whole-rock compositions are reported in Table 2 and Fig. S5. Samples of Bielsa exhibit similar composition, typical of granodiorite, except for samples ZAL18-14A (dioritic composition) and ZAL18-17A and ZAL18-17B that include Qz-rich veins. Following the plutonic total alkali silica classification, Maladeta samples are categorized as granites and quartz-monzonites (Fig. S5). The major element composition was plotted against the composition of undeformed samples for each transect (black dot in Fig. 12). Element contents (expressed in wt. % of oxides) were plotted against TiO_2 content (isocon representation is available in Fig. S6, S7 and S8), with Ti considered immobile. This choice is supported by Ti-bearing phases (such as titanite) observed to grow *in-situ* after the breakdown of biotite (Fig. S1a and Airaghi et al., 2020a). Aluminum was also considered for reference: a linear correlation is observed between Al_2O_3 and TiO_2 (correlation coefficient = 0.7 for Bielsa and 0.6 for Maladeta), but relative variations of Al_2O_3 are higher than those of TiO_2. Hereafter, increases in concentration relative to TiO_2 are interpreted as gains, and decreases as losses from the system. Variations are referred to the undeformed protolith.

In samples of transect B1, MgO, FeO and MnO correlate positively with TiO_2. Larger variations are observed for Na_2O, K_2O and CaO contents, with systematic decrease in Na_2O with increasing deformation (up to -75 %, Table 2). Lowest value for K_2O (-47 %) are obtained in the highest strain sample while highest values (+13 %) in the medium strain samples (Fig. 12 and Table 2). The content in CaO is highly variable across the transect (from -89 % to + 135 %), with the highest enrichment in the medium and high strain samples (Table 2). Mylonites from transect B2 share similar characteristics to B1, except that they exhibit depletion in SiO_2 (-22 %), they are more strongly depleted in Na_2O (-88

%) and they are K-enriched (+ 10 %, Fig. 12, Table 2). For minor and trace elements, a loss of ~ 50 % of Sr is observed in both transects of the Bielsa granitoid, from undeformed samples to mylonites. In the B1 transect, Sr, Be and Ga contents decrease with increasing strain but Rb, Th and Ni contents increase. No significant variations affect other trace elements. In the B2 transect, a general increase of trace elements (Ba, Be, Cs, Hf, Nb, Sc, Y, Zr) is instead observed with increasing strain (Tables S3, Fig. S6 and S7). No major variations in REE occur in deformed samples of the B1 transect, while in B2 a slight enrichment in REE (especially in La, Cs, Pr, Nd) is observed with increasing strain (Table S4, Fig. S6 and S7). Volatile content (as shown by loss on ignition, inferred from the mineralogy as mainly originating from H_2O and CO_2) increases with increasing deformation (Table 2).

In Maladeta, variations of major element concentrations with increasing strain are smaller (± 15-20 % maximum, Fig. 12, Table 1), except for Ca (± 20-40 % in average and up to ± 90 % in sample ZAL18-19B, Table 2). Other major element contents are similar to the undeformed granite. Amounts in trace elements and REE of deformed samples along the transect depart within 25 % from the undeformed granite, with little correlation with strain except for a slight decrease in Sc and Ta with increasing strain (Tables S3 and S4, Fig. S8). Volatile contents are two to three times lower than in Bielsa (Table 2) and variations along the transect are smaller than 3 %.

8. Chlorite thermometry

Crystallization temperatures estimated with the thermometer of Bourdelle and Cathelineau (2015) for chlorite in Maladeta samples are in the range of 250-380°C (Fig. 13a), hence largely overlapping with the majority of the temperature values estimated with the multi-equilibria approach of Vidal et al. (2006) comprised between 250 and 330°C (Fig. 13b). The estimated Fe^{3+} proportion is comprised between 20 and 30% of the total iron. Temperature values were statistically tested for 3000 random temperature simulations from the estimated temperature series (Figure 13b), assuming a Gaussian error of ± 30°C. Temperature values for Maladeta chlorites (red in Fig. 13a, b) were merged in Figure 13 to the ones obtained for chlorite in the samples of Bielsa (and provided in Airaghi et al., 2020a, grey in Fig. 13a, b).

9. Discussion

9.1 Fluid-rock interactions and element mobility in Bielsa and Maladeta

Geochemical variations in samples from a same transect appear primarily due to fluid-rock interactions, rather than to lithological variations of the protolith (with the exceptions specified above). This is motivated by the similar composition among protoliths, and the correlation of compositional variations with strain and with mineralogy, in particular sericitization. In Bielsa, the lack of correlation between alkalis and other major elements, together with the general loss of Na and gain of K with increasing deformation (due to breakdown of plagioclase and crystallization of white mica) point to an open-system behavior for the high strain samples. Sodium loss with increasing strain is consistent with what is generally observed in shear zones acting as open systems on all metamorphic grades (Tursi et al., 2018). Loss of 74-88 % of Na in high strain samples is also similar (or slightly higher) than what is estimated for crystalline fault cores (e.g. Goddard and Evans, 1994). Variations in K with strain are less systematic than those in Na, as observed in shear zones developed in greenschist-facies conditions (Tursi et al., 2018). This suggests lateral element transfer between high-strain samples and the surrounding granodiorite in addition to net gain, and/and heterogeneous fluid-assisted alteration (as documented down to nanoscale by Airaghi et al., 2020b). The correlated behaviors of Mn, Fe and Mg in the B1 transect are consistent with small migration length-scales for these elements due to the replacement of biotite by chlorite. Relative gain or loss of these elements between samples appear linked to variable proportions of secondary chlorite growing in opening cracks (Airaghi et al., 2020b). In transect B2, variations in the effective mobility of Ca, Fe and Mg between samples may reflect variable composition of the interstitial fluid phase. Transient variations in the fluid composition are consistent with local equilibria observed in low and medium strain samples (Airaghi et al., 2020b). Syn-kinematic percolation of Ca and CO_2-rich fluids is suggested by higher modal proportion of calcite in mylonites than in the undeformed granitoid, and by the abundance of calcite in vein-like samples (e.g. ZAL18-14B).

Rock volume gains and losses across B1 and B2 transects (10-12 %, Fig. S6a and S7a), along with volatile contents increasing with increasing strain, also indicate that Bielsa shear zones experienced

pervasive fluid-rock interactions and mass transfer at least partly during shearing (Alpine compressional phase).

In Maladeta, differences between the composition of the undeformed and deformed samples are interpreted as elemental migration through the deformation zone (following the model of Hippertt et al., 1998), with small net element loss or gain within the shear zone. Absence of significant volume variations (Fig. S8), as well as lower volatile contents than in Bielsa samples, suggest weaker fluid-rock interaction and thus mineral transformations in Maladeta.

In summary, while the Bielsa shear zones evolved under fluid-abundant conditions resulting in high element mobility, the Maladeta shear zone records local mass transfer in a more fluid-deficient system. Hence, different geochemical behaviors are observed in these shear zones formed in similar protoliths, at the same time and at similar low greenschist-facies metamorphic conditions.

9.2 Temperature conditions during deformation

Temperature values estimated for chlorite crystallization with the thermometers of Bourdelle and Cathelineau (2015) and Vidal et al. (2006) in the Maladeta samples are in the same range as those previously estimated from chlorite of deformed Bielsa granitoids (250-350°C, Fig. 13). Temperatures obtained with the thermometer of Vidal et al. (2006) for Maladeta samples are slightly lower than for Bielsa. Differences might be due to the simultaneous estimation of Fe^{3+} in the model of Vidal et al. (2006) while all iron is considered as Fe^{2+} in the thermometer of Bourdelle and Cathelineau (2015), even if chlorite in Maladeta is generally more Fe-rich (30-31 wt.% FeO_{tot}) than in Bielsa samples (~ 25 wt. %, Airaghi et al., 2020a). The XFe^{3+} calculated for chlorite of Maladeta with the model of Vidal et al. (2006) is in the same range (0.2-0.3 of Fe_{tot}) of XFe^{3+} measured in chlorite formed in samples of Bielsa that are analogous to the ones studied here (0.20-0.27 of Fe_{tot}, see Airaghi et al., 2020b). Scattered values at low temperature (T < 230°C in Fig. 13) in the model of Vidal et al. (2006) could be attributed to modeling uncertainties due to Fe^{3+} and/or to some starting composition of chlorite from equilibrium with assumed unit activity for quartz and water. Temperature range obtained with the thermometer of Bourdelle and Cathelineau (2015) is also similar between the two massifs (with 90 % of the data comprised between 250 and 350°C), consistent with the similarity of the metamorphic reactions

observed as sericitization of feldspar and chloritization of biotite. Although differences of some tens of degrees between the two massifs cannot be resolved with chlorite thermometry, slightly higher temperature in Maladeta are suggested by ZFT ages, resetted during Cenozoic time, in contrast to Bielsa (Waldner et al., 2021).

9.3 Relationship between mineralogy, temperature of shearing, quartz textures and strain accommodation

Microscopic observations and EBSD data show different microstructures and mechanisms of quartz reworking and different mechanisms of strain accommodation in Bielsa and Maladeta shear zones. In Bielsa, fracturing of quartz dominates over plastic deformation. Thin, straight misoriented bands in Qz1 of high strain samples (white arrows Fig. 9b) are interpreted as incipient microcracks that may evolve into localized shear bands as the ones described by van Daalen et al. (1999). Weak plastic deformation of Qz1 is observed coexisting with brittle deformation. Narrow and wide deformation bands (NDB and WDB) recall fine and wide extinction bands (FEB and WEB) described by Derez et al. (2015) that indicate low grade (consistent with T < 350°C estimated in our samples) crystal plastic mechanisms. Processes other than dynamic recrystallization, such as mass transfer through dissolution-reprecipitation and/or nucleation and growth, better explain the behavior of Qz2 grains, possibly combined with microporosity evolution (e.g. Fusseis et al., 2009; Gilgannon et al., 2017). This is motivated by the facts that Qz2 grains are mainly isolated in matrix mica (± calcite) and never associated to polygonal subgrains in Qz1, and quartz does not show clear CPO. The very weak fabric is also consistent with a combination of minor dislocation creep and dominant pressure-solution creep processes. Non-coaxial strain is mainly accommodated in the weak mica-rich matrix.

In Maladeta, (re)crystallization of Qz2 is higher than in Bielsa. The similarity in shape and size between Qz2 and polygonal subgrains in Qz1 and typical core-mantle structures indicate that Qz2 grains result – at least partly – from progressive misorientation of subgrains (White, 1979). The recrystallization mechanism inferred is subgrain rotation. Recrystallized Qz2 grains aligned along misoriented shear bands within Qz1 recall recrystallized quartz grains formed from rhombohedral quartz

fragments broken off and rotated along initial microcracks (van Daalen et al., 1999; Kjøll t al., 2015). Quartz grains aligned along intragrain fractures may attest of either the rotation of fragment and subsequent nucleation of new grains or a precipitation from a free fluid film circulating in intragrain cracks (Kjøll et al., 2015), along subgrain boundaries, or in zones of high dislocation densities as shown by KAM maps (Hippertt and Egydio-Silva, 1996; Précigout et al., 2022). This indicates conditions favoring coexisting brittle and plastic deformation in the Maladeta shear zone. The low *J*- and *M*-indices, the co-existence of different slip systems and the low aspect ratio (Table 1) of quartz aggregates despite pervasive recrystallization suggest that the overall plastic deformation of quartz remains weak and that other processes as dissolution-reprecipitation and/or quartz nucleation may occur coevally with subgrain rotation. The oblique orientation of the CPO fabric relative to the kinematic framework maybe due to the fact that the fabric is quite weak and is also consistent with the occurrence of other processes than dynamic recrystallization leading to the growth of Qz2. The lacking predominance of a given slip system might instead be locally due to inherited CPO with respect to the kinematic reference frame (Menegon et al., 2011; Ceccato et al., 2017). Although strain is mainly accommodated in the matrix, in contrast to Bielsa, quartz in the Maladeta samples exhibits plastic deformation, dynamic recrystallization and more extensive reworking. The transition from quartz fracturing to recrystallization by subgrain rotation occurs between 350 and 380°C, which are the upper limits of synkinematic temperatures estimated for Bielsa and Maladeta, respectively. This temperature range corresponds to the one in which quartz recrystallizes by bulging and not by subgrain rotation (usually described below 400-500°C for differential stresses of 30-50 MPa and similar strain rates; Stipp et al., 2002). Bulging is however almost absent in Maladeta samples.

From these observations we infer that differences in quartz microstructures and extent of quartz recrystallization between Bielsa and Maladeta may be due to one of a combination of the following factors:

(i) difference in fluid content. Wet quartz recrystallizes more easily than dry quartz under equivalent strain (Palazzin et al., 2018). However, in Maladeta samples, where the recrystallization of quartz is extensive, the density of fluid inclusion in parent quartz appears lower than in Bielsa.

Furthermore, controversies exist on the role of fluid in the development of intracrystalline plasticity (as dislocations glide) and quartz strength (Ceccato et al., 2022);

(ii) a difference of some tens of degrees in temperature (higher in Maladeta, see 9.2). In this case, deformation of quartz and recrystallization textures appear overly sensitive to temperature variation in a range where subgrain rotation is not expected to occur;

(iii) difference in the bulk mica-quartz ratio and extent of mixing of mica and quartz grains (e.g. Graziani et al., 2020). In Bielsa, the presence of 40-50 % vol. of mica and more pervasive phase mixing results in strain accommodation only in the matrix, and therefore little quartz recrystallization. This has also been observed experimentally by Tullis and Wenk (1994). In Maladeta, a lower amount of mica (20-28 % vol.) and the preservation of quartz aggregates result in more extensive quartz recrystallization, with strain being also accommodated in quartz.

No quantitative constraints are available for strain rates in the two massifs, but the similarity in grain size of minor quartz recrystallized by bulging in Maladeta (ZAL18-20E, 9.00 ± 0.54 μm) and in Bielsa in the rare localities where incipient bulging is observed suggests similar ranges of differential stress (Stipp et al., 2002; Cross et al., 2017).

9.4 Role of pre and syn-kinematic fluid-rock interactions on mica-quartz mixing, quartz recrystallization and structural style of Bielsa and Maladeta

Petrographic and geochemical results indicate that Bielsa samples experienced higher fluid-rock interactions than Maladeta samples. While at least part of the alteration in Bielsa occurred during the Permian-Triassic (230-300 Ma, Airaghi et al., 2020a), no absolute time constraints are yet available for the hydrothermal alteration of the Maladeta granite. Yet, whole-rock compositions of Maladeta samples slightly, but systematically evolve with increasing deformation. This suggests that fluid-rock interaction in Maladeta is mainly related to Alpine deformation. Changes in REE concentration within shear zones have been previously related to the alteration of the magmatic REE-bearing minerals during fluid-rock interaction events, rather than to strain intensity, deformation and shear zone mineral assemblage

(Rolland et al., 2003). Higher variations in REE (for B2 transect) and in trace elements in Bielsa, along with the extensive mineralogical transformations in undeformed samples point to a more pervasive pre-kinematic (pre-Alpine shearing) alteration in Bielsa than in Maladeta rocks. The lack of correlation between trace element contents and the strain gradient in Bielsa also suggests that compositional differences were acquired during fluid-rock interactions before Alpine shearing. More pervasive pre-kinematic hydrothermal alteration in Bielsa than in Maladeta partly explains higher mica-quartz mixing. While a minor amount of excess silica arose from feldspar sericitization precipitated at the reaction sites (Fig. 5) within dilatant pores (as observed by Knipe and Wintsch, 1985; Wibberley, 1999), pre-kinematic alteration in Bielsa increased the porosity of the granite (Airaghi et al., 2020b), giving rise to microstructural sites for white mica to nucleate. This process, along with microfracturing (Airaghi et al., 2020b), increased the efficiency of fluid infiltration during shearing and favored further fluid-rock interactions and phyllosilicate crystallization (as observed in similar contexts by Kerrich et al., 1980; McCaig et al., 1984; McCaig et al., 1990; Marquer et al., 1994; Rolland and Rossi., 2016). This contributed to the redistribution of mineral phases at the scale of ~100 µm.

The similar to slightly higher temperature of shearing in Maladeta contrast with more distributed deformation (e.g. Gapais and Balé, 1990) in the granitic massif of Bielsa. Therefore, pre-conditioning of the granitic protolith due to the pre-kinematic alteration, appears as the key factor of strain localization and accommodation. The growth of larger amounts of mica and pervasive quartz-mica mixing during the Permian-Triassic alteration in Bielsa also affected the mechanisms of deformation and reworking of quartz (as also observed in the felsic lower crust, Graziani et al., 2020). This may account for strain to be more distributed than in Maladeta at a microscropic scale, as suggested for various greenschist-facies granitic shear zones of multiple geological settings (e.g. Menegon et al., 2008; Spruzeniece and Piazolo, 2015).

If generalized in the massifs, the small scale processes described above may control strain distribution at the mesoscopic scale, resulting in more pervasive deformation in the Bielsa granitoid than in Maladeta. Beyond very local lithological heterogeneities (ZAL18-14A), the location and density of shear zones may have been controlled by Late-Variscan structural heterogeneities, that caused heterogeneous fluid-rock interactions and therefore, heterogeneous phyllosilicate growth before and

during shearing (differences of only 10-20 % in the proportion of phyllosilicates were proposed to control the sites of shear zone nucleation in alpine granites, Wehrens et al., 2016). Alpine brittle precursors, as observed at the mm-scale forming fractures filled with calcite, Alpine white mica and chlorite (Wm2 and Chl2 in Airaghi et al., 2020a) could also favor further mineral reaction and phyllosilicate growth. This probably favored shear zone development, as observed in numerous granitic shear zones in the Alps (Guermani and Pennacchioni, 1998; Mancktelow and Pennacchioni, 2005; Pennacchioni and Mancktelow, 2007).

10. Conclusion

Greenschist-facies shear zones of the Bielsa and Maladeta granitoids (Axial zone, Pyrenees) show different structural styles (distributed *vs* localized shear zones) and microstructures, despite having similar lithologies, tectonic and syn-kinematic histories. Based on microstructural analysis and geochemical results, we explain this discrepancy by reconstructing the post-Variscan geological history of the two massifs as follows:

1. The shear zones of Bielsa evolved under fluid-abundant conditions while the shear zone in Maladeta evolved under fluid-limited conditions with only local mass transfer. The Bielsa granite experienced more pervasive pre-kinematic (Late-Variscan) fluid-rock interactions than in Maladeta. This is shown by extensive alteration of the magmatic mineral assemblage in Bielsa, higher matrix-porphyroblasts ratios, as well as larger variations in major element composition in high strain samples of Bielsa (± 20-70%) compared to Maladeta (± 15-20%).

2. In shear zones of Bielsa, quartz porphyroclasts are mainly fractured. Reworking of quartz is minor and occurs mainly by dissolution-reprecipitation. In contrast, quartz exhibits higher plastic deformation

in the shear zones of Maladeta. Reworking of quartz grains is pervasive and occurs by recrystallization by subgrain rotation, dissolution-reprecipitation and nucleation in microcracks.

3. The evolution from a regime where quartz is fractured to a regime where quartz deforms plastically and recrystallizes by subgrain rotation occurs in a narrow range of ~30°C (at 350-380°C), well below the previously suggested 450°C. In addition, almost no bulging recrystallization is observed at the transition between fracturing and subgrain rotation.

4. Stronger recrystallization of quartz occurs in the fluid-deficient and slightly hotter Maladeta shear zone. This appears to be in contrast with more intense strain localization at the larger scale. Fluid availability and mineralogy appear therefore as key factors to explain differences in strain distribution, micro- and meso-textures, as shown in shear zones from the two massifs.

5. Pervasive alteration in Bielsa during Permian-Triassic (Late-Variscan) and fluid-abundant conditions during the Alpine compressional stage promoted the growth of larger amounts of mica (40-50 vol. %), and the deformation and recrystallization of quartz. Weaker alteration in Maladeta during Late-Variscan, and more fluid-deficient conditions during the Alpine compressional stage limited the growth of mica (20-28 vol. %) and phase mixing. This promoted quartz deformation and recrystallization since strain is not entirely accommodated by the mica-rich matrix.

Acknowledgements

This study was founded by the CNRS-BRGM-TOTAL 'OROGEN' project. We thank Michel Fialin, Nicolas Rividi and Omar Boudouma for their help with electron microscopy and electron microanalyser of ISTeP. We acknowledge Benoit Caron and Benoît Villemant for their support with ICP-OES and ICP-MS analytical techniques. We are grateful to Samuel Angiboust for his careful editorial handling. Alberto Ceccato, Yann Rolland and Fabrizio Tursi are thanked very much for their constructive reviews.

References

Abd Elmola, A., Buatier, M., Monié, P., Labaume, P., Trap, P., & Charpentier, D. (2018). 40Ar/39Ar muscovite dating of thrust activity: a case study from the Axial Zone of the Pyrenees. Tectonophysics, 745, 412-429

Airaghi, L., Bellashen, B., Dubacq, B., Chew, D., Rosenberg, C., Janots, E., Waldner, M. & Magnin, V. (2020a). Pre-orogenic upper crustal softening by lower greenschist-facies metamorphic reactions in granites of central Pyrenees. Journal of Metamorphic Geology 38(2), 183–204.

Airaghi, L., Dubacq, B., Verlaguet, A., Bourdelle, F., Bellahsen, N. & Gloter, A. (2020b). From static alteration to mylonitization: a nano-to micrometric study of chloritization in granitoids with implications for equilibrium and percolation lenghtscales. Contributions to Mineralogy and Petrology, 175:108.

Alderton, D.M.H., Pearce, J.A., Potts, P.J. (1980). Rare earth element mobility during granite alteration: evidence from Southwest Englang. Earth and Planetary Science Letters, 49, 149-165.

Bellahsen N., Bayet, L., Denele, Y., Waldner, M., Airaghi, L., Rosenberg, C., Dubacq, B., Mouthereau, F., Bernet, M., Pik, R., Lahfid, A., Vacherat, A. (2019). Shortening of the Axial Zone, Pyrenees: shortening sequence, upper crustal mylonites and crustal strength. Tectonophysics.

Bourdelle, F., Parra, T., Chopin, C., & Beyssac, O. (2013). A new chlorite geothermometer for diagenetic to low-grade metamorphic conditions. Contributions to Mineralogy and Petrology, 165(4), 723-735.

Bourdelle, F. and Cathelineau, M. (2015). Low-temperature chlorite geothermometry: a graphical representation based on a T-R^{2+}-Si diagram. European Journal of Mineralogy, 27, 617-626.

Bunge, H. J. (1982). Texture analysis in materials science: mathematical methods. Elsevier.

Casas, A. M., Oliva, B., Román-Berdiel, T., & Pueyo, E. (2003). Basement deformation: Tertiary folding and fracturing of the Variscan Bielsa granite (Axial zone, central Pyrenees). Geodinamica Acta, 16(2–6), 99–117. https://doi.org/10.1016/j.geoact.2003.09.001

Ceccato, A., Pennacchioni, G., Menegon, L. & Bestmann, M. (2017). Crystallographic control and texture inheritance during mylonitization of coarse grained quartz veins. Lithos, 290-291, 210-227.

Ceccato, A., Goncalves, P., & Menegon, L. (2022). On the petrology and microstructures of small-scale ductile shear zones in granitoid rocks: An overview. Journal of Structural Geology, 104667.

Cenki-Tok, B., J. R. Darling, Y. Rolland, E. Dhuime, and C. D. Storey (2014), Direct dating of mid-crustal shear zones with synkinematic allanite: New in situ U-Th-Pb geochronological approaches applied to the Mont Blanc massif, Terra Nova, 26(1), 29– 37.

Cochelin, B., Chardon, D., Denèle, Y., Gumiaux, C., & Le Bayon, B. (2017). Vertical strain partitioning in hot Variscan crust: Syn-convergence escape of the Pyrenees in the Iberian-Armorican syntax. BSGF-Earth Sciences Bulletin, 188(6), 39.

Cross, A. J., Prior D. J., Stipp M., & Kidder S. (2017). The Recrystallised Grain Size Piezometer for Quartz: An EBSD-Based Calibration: EBSD-Based Quartz Grain Size Piezometer. Geophysical Research Letters 44(19), 6667–74.

Derez, T., Pennock, G., Drury, M. & Sintubin, M; (2015). Low-temperature intracrystalline deformation microstructures in quartz. Journal of Structural Geology, 71, 3-23.

Etheridge, M. A., and Wilkie, J. C. (1979). Grainsize reduction, grain boundary sliding and the flow strength of mylonites. Tectonophysics, 58(1-2), 159-178.

Fitz Gerald, J. D., & Stünitz, H. (1993). Deformation of granitoids at low metamorphic grade. I: Reactions and grain size reduction. Tectonophysics, 221(3-4), 269-297.

Fusseis, F., Regenauer-Lieb, K., Liu, J., Hough, R. M., & De Carlo, F. (2009). Creep cavitation can establish a dynamic granular fluid pump in ductile shear zones. Nature, 459(7249), 974-977.

Gapais, D. & balé, P. (1990). Shear zone pattern and granite empalcement within a Cadomian sinistral wrench zon at St Cast, N. Brittany. Geological Society of London, Special Publications, 51, 169-179.

Gilgannon, J., Fusseis, F., Menegon, L., Regenauer-Lieb, K., & Buckman, J. (2017). Hierarchical creep cavity formation in an ultramylonite and implications for phase mixing. Solid Earth, 8(6), 1193-1209.

Glanzer, A. F. and Bartley, J. M. (1991). Volume loss, fluid flow and state of strain in extensional mylonites from the central Mojave Desert, California. Journal of Structural Geology, 13(5), 587-

594.
Goddard, J. V. & Evans, J. P. (1995). Chemical changes and fluid-rock interaction in faults of crystalline thrust sheets, northwestern Wyoming, U.S.A. Journal of Structural Geology, 17(4), 553-547.
Goncalves, Philippe, Poilvet, J. C., Oliot, E., Trap, P., & Marquer, D. (2016). How does shear zone nucleate? An example from the Suretta nappe (Swiss Eastern Alps). Journal of Structural Geology, 86, 166–180.
Grant, J. A. (1986). The isocon diagram; a simple solution to Gresens' equation for metasomatic alteration. Economic geology, 81(8), 1976-1982.
Graziani, R., Larson, K. P. and Soret, M. (2020). The effect of hydrous mineral content on competitive strain localization mechanisms in felsic granulites. Journal of Structural Geology, 134, 104015.
Guermani, A., & Pennacchioni, G. (1998). Brittle precursors of plastic deformation in a granite: an example from the Mont Blanc massif (Helvetic, western Alps). Journal of Structural Geology, 20(2-3), 135-148.
Gueydan, F., Leroy, Y. M., Jolivet, L. & Agard, P. (2003). Analysis of continental midcrustal strain localization induced by microfracturing and reaction-softening. Journal of Geophysilical Research, 108(B2), 2064.
Halfpenny, A., Prior, D. J., & Wheeler, J. (2012). Electron backscatter diffraction analysis to determine the mechanisms that operated during dynamic recrystallisation of quartz-rich rocks. *Journal of Structural Geology*, *36*, 2-15.
Herwegh, M., Linckens, J., Ebert, A., Berger, A., & Brodhag, S. H. (2011). The role of second phases for controlling microstructural evolution in polymineralic rocks: A review. Journal of Structural Geology, 33(12), 1728-1750.
Hippertt, J.F. & Egydio-Silva, M. (1996). New polygonal grains formed by dissolution-redeposition in quartz mylonite. Journal of Structural Geology, 18(11), 1345-1352.
Hippertt, J.F. (1998). Breakdown of Feldspar, Volume Gain and Lateral Mass Transfer during Mylonitization of Granitoid in a Low Metamorphic Grade Shear Zone. Journal of Structural Geology 20(2–3), 175–93.
Hunter, N. J. R., Hasalová, P., Weinberg, R. F. & Wilson, C. J. L. (2016). Fabric controls on strain accomodation in naturally deformed mylonites: The influence of interconnected micaceous layers. Journal of Structural Geology, 83, 180-193.
Jolivet, M., Labaume, P., Monié, P., Brunel, M., Arnaud, N., & Campani, M. (2007). Thermochronology constraints for the propagation sequence of the south Pyrenean basement thrust system (France-Spain). Tectonics, 26(5).
Kerrich, R., Allison, I., Barnett, R. L., Moss, S., & Starkey, J. (1980). Microstructural and chemical transformations accompanying deformation of granite in a shear zone at Mieville, Switzerland; with implications for stress corrosion cracking and superplastic flow. Contributions to Mineralogy and Petrology, 73(3), 221-242.
Kilian, R. and Heilbronner, R. (2017). Analysis of crystallographic preferred orientations of experimentally deformed Black Hills Quartzite. Solid Earth, 8, 1095-1117.
Kjøll, H. J., Viola, G., Menegon, L., & Sørensen, B. E. (2015). Brittle–viscous deformation of vein quartz under fluid-rich lower greenschist facies conditions. Solid Earth, 6(2), 681-699.
Knipe, R.J. and Wintsch, R.P. (1985). Heterogeneous, deformation, foliation development, and metamorphic processes in a polyphase mylonite. In: Thompson, A.B., Rubie, D.C. (Eds.), Advances in Physical Chemistry, vol. 4. Springer-Verlag, New York, pp. 180-210.
Mancktelow, NS. & Pennacchioni, G. (2005). The control of precursor brittle fracture and fluid-rock interaction on the development of single and paired ductile shear zones. Journal of Structural geology, 27(4), 645-661.
Marquer, D., Petrucci, E. & Iacumin, P. (1994). Fluid advection in shear zones: evidence from geological and geochemical relationships in the Aiguilles Rouges Massif (Western Alpes, Switzerland). Scheiz. Mineral. Petrogr. Mitt. 74, 137-148.
Menegon, L., Pennacchioni, G., Heilbronner, R. & Pittarello, L. (2008). Evolution of quartz microstructure and c-axis crystallographic preferred orientation within ductilely deformed granitoids (Arolla unit, Western Alps), Journal of Structural Geology, 30, 1332-1347.
Menegon, L., Piazolo, S. & Pennacchioni, G. (2011). The effect of Dauphiné twinning on plastic strain in quartz. Contrib Mineral Petrol, 161, 635-652.

McCaig, A. M. (1984). Fluid-rock interaction in some shear zones from the Pyrenees. Journal of Metamorphic Geology, 2(2), 129-141.

McCaig, A. M., Wickham, S. M., Hugh, P. and Taylor, Jr. (1990). Deep fluid circulation in alpine shear zones, Pyrenees, France: field and oxygen isotope studies. Contributions to Mineralogy and Petrology, 106, 41-60.

Metcalf, J. R., Fitzgerald, P. G., Baldwin, S. L., & Muñoz, J. A. (2009). Thermochronology of a convergent orogen: Constraints on the timing of thrust faulting and subsequent exhumation of the Maladeta Pluton in the Central Pyrenean Axial Zone. Earth and Planetary Science Letters, 287(3–4), 488–503.

Michard-Vitrac, A., Albarede, F., Dupuis, C., & Taylor, H. P. (1980). The genesis of Variscan (Hercynian) plutonic rocks: Inferences from Sr, Pb, and O studies on the Maladeta igneous complex, central Pyrenees (Spain). Contributions to Mineralogy and Petrology, 72(1), 57–72.

Middlemost, E. A. (1994). Naming materials in the magma/igneous rock system. *Earth-science reviews*, *37*(3-4), 215-224.

Muñoz, J.A. (1992) Evolution of a continental collision belt: ECORS-Pyrenees crustal balanced cross-section. In: McClay KR (ed) Thrust tectonics. Springer, Dordrecht, 235-246.

O'Hara, K. (1988). Fluid flow and volume loss during mylonitization: an origin for phyllonite in an overthrust setting, North Carolina USA. Tectonophysics, 156(1-2), 21-36.

Palazzin, G., Raimbourg, H., Stünitz, H., Heilbronner, R., Neufeld, K. and Précigout, J. (2018). Evolution in H2O contents during deformation of polycrystalline quartz: An experimental study. Journal of Structural Geology, 114, 95-110.

Pennacchioni, G. & Mancktelow, NS. (2007). nucleation and initial growth of a shear zone network within compositionally and structurally heterogeneous granitoids under amphibolite facies conditions. Journal of Structural Geology, 29(11), 1757-1780.

Piazolo, S., Bons, P.D., Jessell, M.W., Evans, L. and Passchier, C.W. (2002). Dominance of microstructural processes and their effects on microstructural development: insights from numerical modelling of dynamic recrystallization. Geological Society of London Speical Publications, 200(1), 149-170.

Pouchou, J. L., & Pichoir, F. (1991). Quantitative analysis of homogeneous or stratified microvolumes applying the model "PAP". In Electron probe quantitation (pp. 31-75). Springer, Boston, MA.

Précigout, J., Prigent, C., Palasse, L. & Pochon, A. (2017) Water pumping in mantle shear zones. Nature communications, 8: 15736.

Précigout, J., Stünitz, H. & Villeneuve, J. (2019) Excess water storage induced by viscous strain localization during high-pressure shear experiment. Scientific Reports, 9(1): 3463.

Précigout, J., Ledoux, E., Arbaret, L. and Spriet, C. (2022). Porosity induced by dislocation dynamics in quartz-rich shear bands of granitic rocks. Scientific reports,12: 6141.

Rolland, Y., Cox, S., Boullier, A.-M., Pennacchioni, G., & Mancktelow, N. (2003). Rare earth and trace element mobility in mid-crustal shear zones: insights from the Mont Blanc Massif (Western Alps). Earth and Planetary Science Letters, 214(1–2), 203–219.

Rolland, Y. & Rossi, M. (2016). Two-stage fluid flow and element transfers in shear zones during collision burial-exhumation cycles: insights from the Mont Blanc crystalline Massif (Western Alps). Journal of Geodynamics, 101, 88-108.

Román-Berdiel, T., Casas, A. M., Oliva-Urcia, B., Pueyo, E. L., & Rillo, C. (2004). The main Variscan deformation event in the Pyrenees: New data from the structural study of the Bielsa granite. Journal of Structural Geology, 26(4), 659–677.

Rossi, M., Rolland, Y., Vidal, O., and Cox, S. F. (2005). Geochemical variations and element transfer during shear-zone development and related episyenites at middle crust depths: insights from the Mont Blanc granite (French—Italian Alps). Geological Society, London, Special Publications, 245(1), 373-396.

Rossi, M., and Y. Rolland (2014), Stable isotope and Ar/Ar evidence of prolonged multiscale fluid flow during exhumation of orogenic crust: Example from the Mont Blanc and Aar massifs (NW Alps), Tectonics, 33, 1681– 1709, doi:10.1002/2013TC003438.

Roure, F., Choukroune, P., Berastegui, X., Munoz, J.A., Villien, A., Matheron, P., Bareyt, M., Seguret, M., Camara, P. and Deramond, J. (1989) Ecors deep seismic data and balanced cross sections: geometric constraints on the evolution of the Pyrenees. Tectonics, 8, 41-50.

Sinclair, H. D., Gibson, M., Naylor, M., & Morris, R. G. (2005). Asymmetric growth of the Pyrenees revealed through measurement and modeling of orogenic fluxes. American Journal of Science, 305(5), 369-406.

Skemer, P., Katayama, I., Jiang, Z., Karato, S. (2005). The misorientation index: Development of a nex method for calculating the strength of lattice-preferred orientation. Tectonophysics, 411, 157-167.

Stipp, M., Stünitz, H., Heilbronner, R., & Schmid, S. M. (2002). Dynamic recrystallization of quartz: correlation between natural and experimental conditions. Geological Society, London, Special Publications, 200(1), 171-190.

Stöckhert et al., 1999 Stöckhert, B., Wachmann, M., Küster, M., & Bimmermann, S. (1999). Low effective viscosity during high pressure metamorphism due to dissolution precipitation creep: the record of HP–LT metamorphic carbonates and siliciclastic rocks from Crete. Tectonophysics, 303(1-4), 299-319.

Song, W. J. and Ree, J.-H. (2007). Effect of mica on the grain size of dynamically recrystallised quartz in a quartz-muscovite mylonite. Journal of structural Geology, 29, 1872-1881.

Spruzeniece, L. and Piazolo, S. (2015) Strain localization in brittle-ductile shear zones: fluid-aboundant vs. fluid-limited conditions (an example from Wyangala area, Australia). Solid Earth, 6, 881-901.

Trimby, P. W., Prior, D. J., & Wheeler, J. (1998). Grain boundary hierarchy development in a quartz mylonite. Journal of Structural Geology, 20(7), 917-935.

Tursi, F., Festa, V., Fornelli, A., Micheletti, F., & Spiess, R. (2018). Syn-shearing mobility of major elements in ductile shear zones: state of the art for felsic deformed protoliths. Period. Mineral, 87, 289-308.

Tursi, F., Acquafredda, P., Festa, V., Fornelli, A., Langone, A., Micheletti, F., & Spiess, R. (2021). What can high-P sheared orthogneisses tell us? An example from the Curinga–Girifalco Line (Calabria, southern Italy). Journal of Metamorphic Geology, 39(7), 919-944.

Van Daalen, M., Heilbronner, R., Kunze, K. (1999). Orientation analysis of localized shear deformation in quartz fibres at the brittle ductile transition. Tectonophysics, 303, 83-107.

Vidal, O., de Andrade, V., Lewin, E., Munoz, M., Parra, T., & Pascarelli, S. (2006). P–T-deformation-Fe3+/Fe2+ mapping at the thin section scale and comparison with XANES mapping: application to a garnet-bearing metapelite from the Sambagawa metamorphic belt (Japan). Journal of Metamorphic Geology, 24(7), 669-683.

Waldner, M., Bellashen, N., Mouthereau, F., Bernet, M., Pik, R., Rosenberg, C. L. and Balvay, M. (2021). Central Pyrenees mountain building: constraints from new LT thermochronological data from the Axial Zone, Tectonics, 40, 3.

Wayne, D. M., & McCaig, A. M. (1998). Dating fluid flow in shear zones: Rb-Sr and U-Pb studies of syntectonic veins in the Nouvielle Massif, Pyrenees. Geological Society, London, Special Publications, 144(1), 129–135.

Wehrens, P., Baumberger, R., Berger, A. & Herwegh, M. (2016). How is strain localized in a meta-granitoid, mid-crustal basement section? Spatial distribution of deformation in the central Aar massif (Switzerland). Journal of Structural Geology, 94, 47-67.

White, S.H. (1979). Subgrain and grain size variation across a shear zone. Contributions to Mineralogy and Petrology, 70, 193-202.

Whitney, D. L., & Evans, B. W. (2010). Abbreviations for names of rock-forming minerals. American Mineralogist, 95(1), 185–187. https://doi.org/10.2138/am.2010.3371

Wibberley, C. (1999). Are feldspar-to-mica reactions necessarily reaction-softening processes in fault zones? Journal of Structural Geology, 21(8–9), 1219–1227.

Wintsch, R. P., Christoffersen, R. & Kronenberg, A. K. (1995). Fluid-rock reaction weakening of fault zones. Journal of Geophysical Research, 100(B7), 13021-13032.

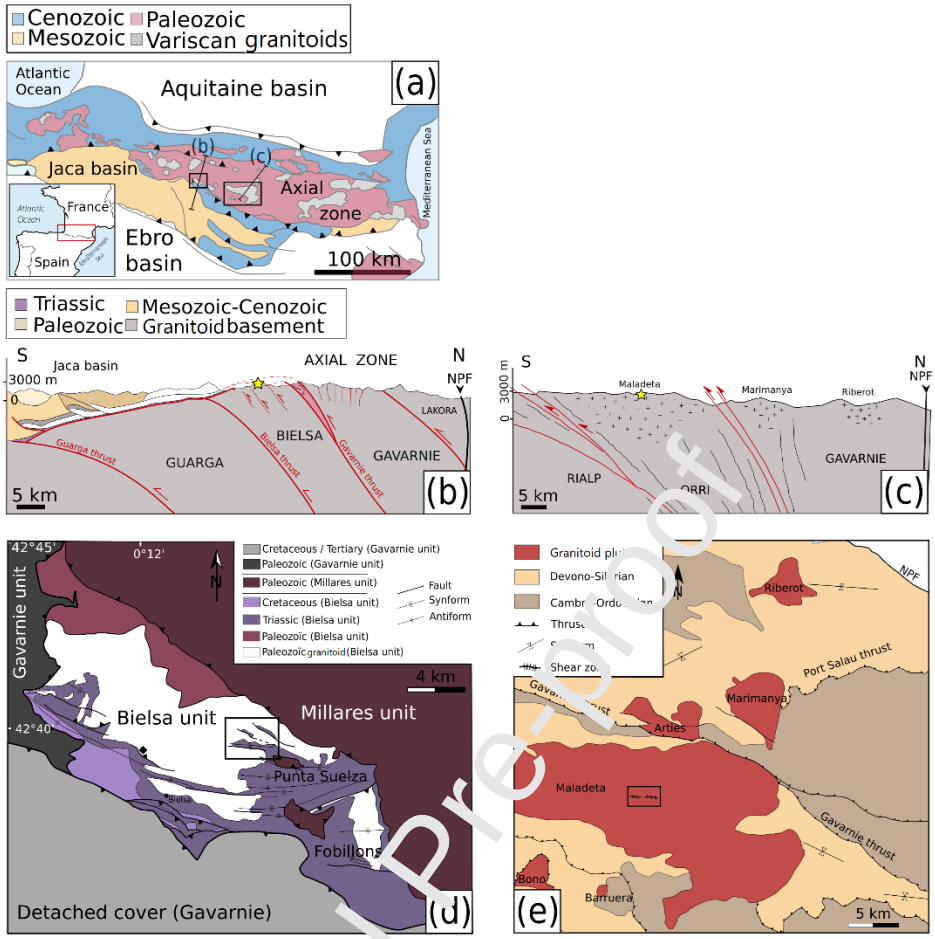

Figure 1 Geological maps and cross sections of the studied areas in the Pyrenees. (a) Simplified geological map of the Pyrenees (modified from Airaghi et al. 2020a). Black squares indicate Bielsa and Maladeta massifs. (b) Bielsa and (c) Maladeta cross-sections (modified from Airaghi et al., 2020a and Waldner et al., 2021). (d) Geological map of the area of Lake of Urdiceto in Bielsa (modified from Bellahsen et al., 2019). (e) Geological map of Maladeta massif. Black square: studied area.

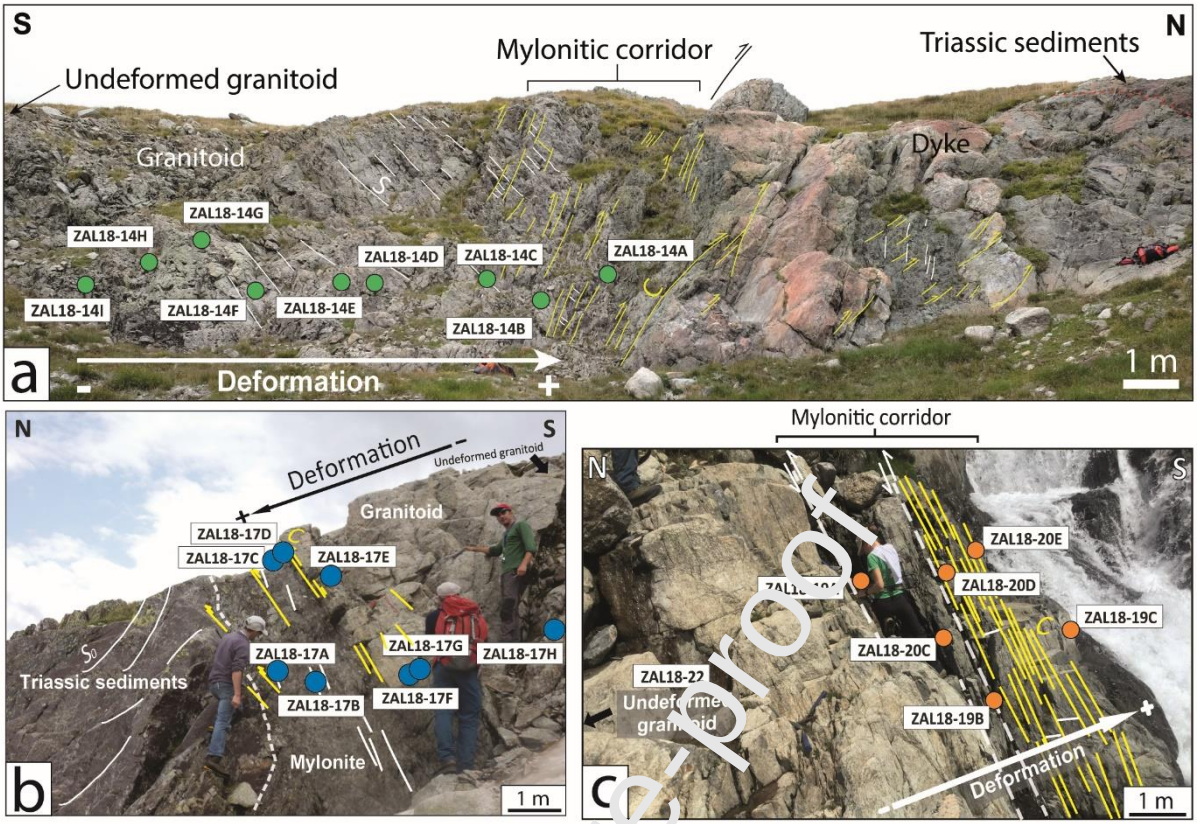

Figure 2 Field view of studied transects with emplacements of samples. (a) Bielsa B1, (b) B2 transects (modified from Airaghi et al., 2020a), (c) Maladeta transect.

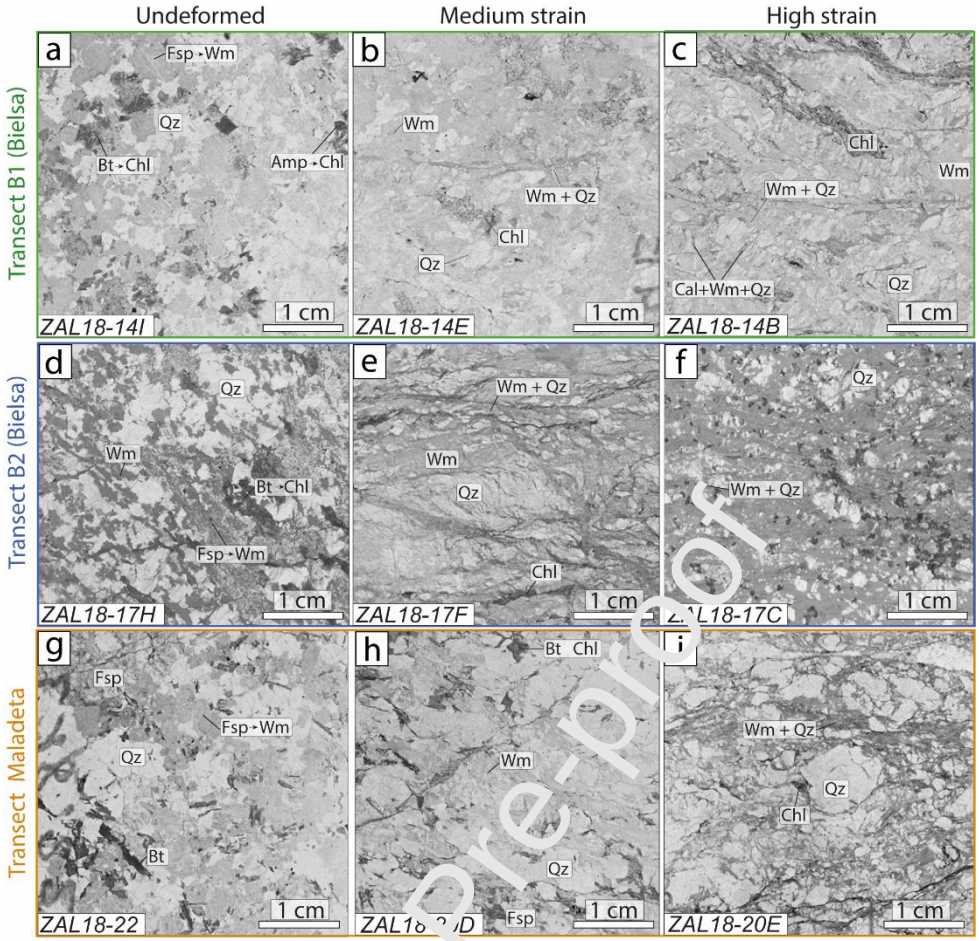

Figure 3 Microscopic views of representative undeformed (a, d, g), medium strain (b, e, h) and high strain samples (c, f, i) for B1, B2 and Maladeta transects. Mineral abbreviations are from Whitney and Evans (2010).

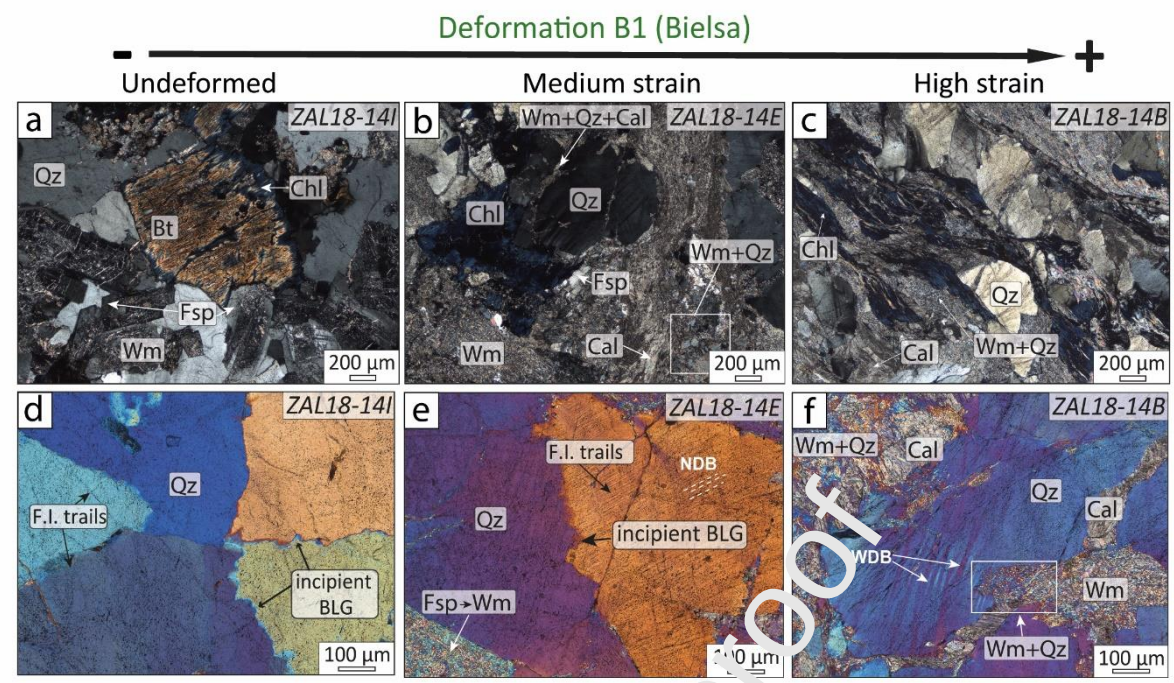

Figure 4 Microviews of samples in B1 transect, from undeformed granitoid (left) to high strain samples (right). (a), (b) and (c) Plane transmitted light image of samples ZAL18-14I, ZAL18-14E and ZAL18-14B, respectively. (d), (e), (f) Microviews showing quartz recrystallization and deformation features under cross-polarised light with lambda plate for the same samples. BLG: bulging, NDB: narrow deformation bands, WDB: wide deformation bands, F.I.: fluid inclusions.

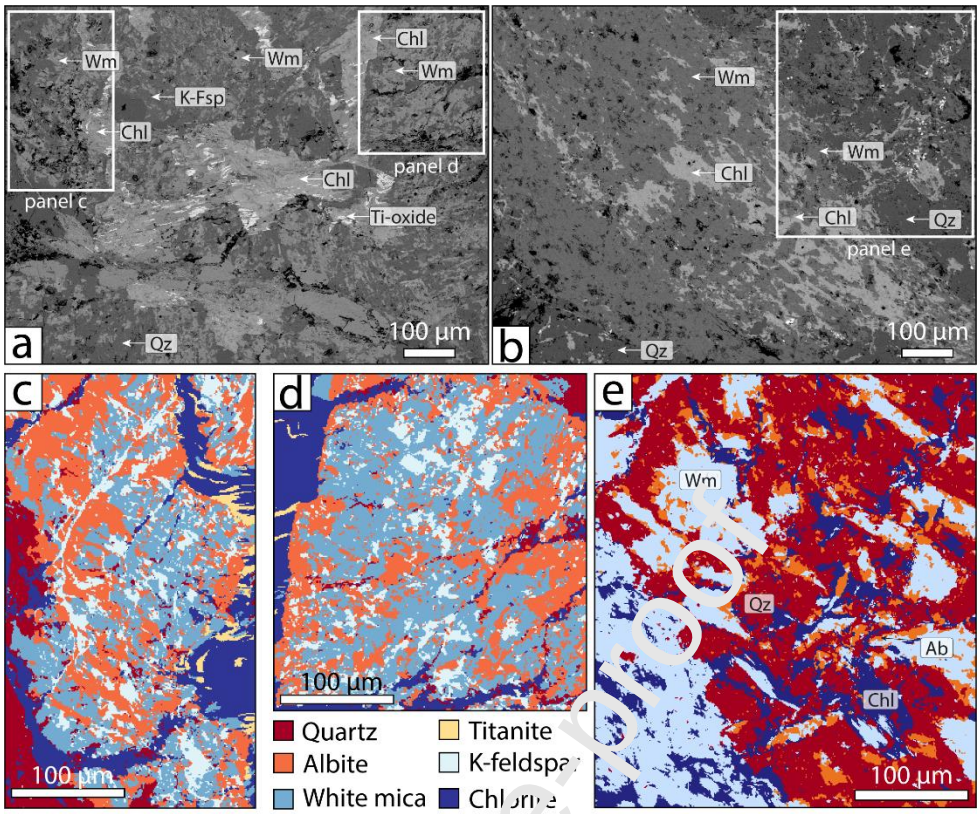

Figure 5 Phase distribution in undeformed sample of B1 transect (ZAL18-14I). (a) and (b) Backscattered electron (BSE) images showing feldspar breakdown. (c), (d) and (e) associated phase maps.

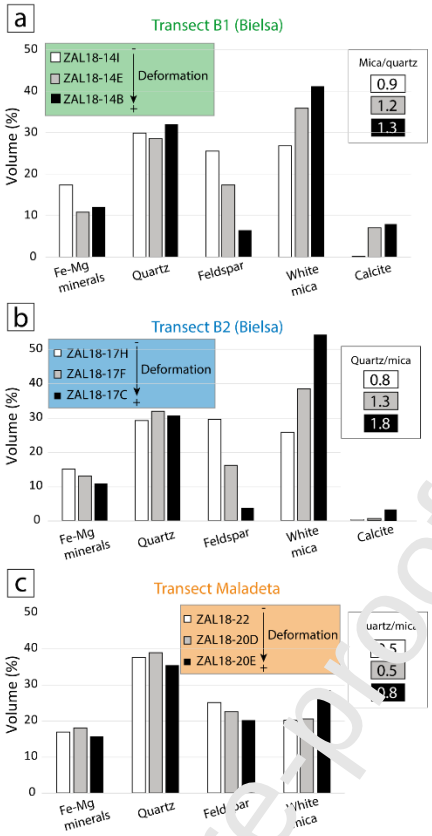

Figure 6 Proportion of mineral phases and mica-quartz ratio in B1 (a), B2 (b) and Maladeta (c) transects. See main text for details. Feldspar includes alkali feldspar and plagioclase.

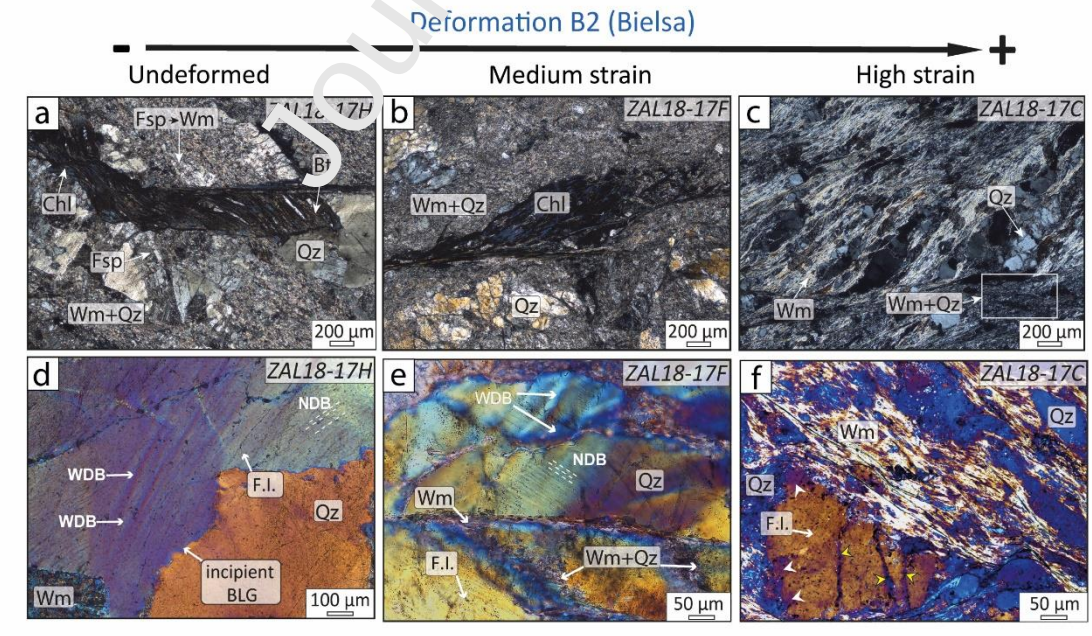

Figure 7 Microviews of samples in B2 transect, from undeformed granitoid (left) to high strain samples (right). Plane transmitted light image of sample ZAL18-17H, ZAL18-17F and ZAL18-17C, respectively. (d), (e) and (f) Microviews showing quartz recrystallization and deformation features under cross-polarised light with lambda plate for the same samples. BLG: bulging, NDB: narrow deformation bands, WDB: wide deformation bands, F.I.: fluid inclusions. White and yellow arrows see text.

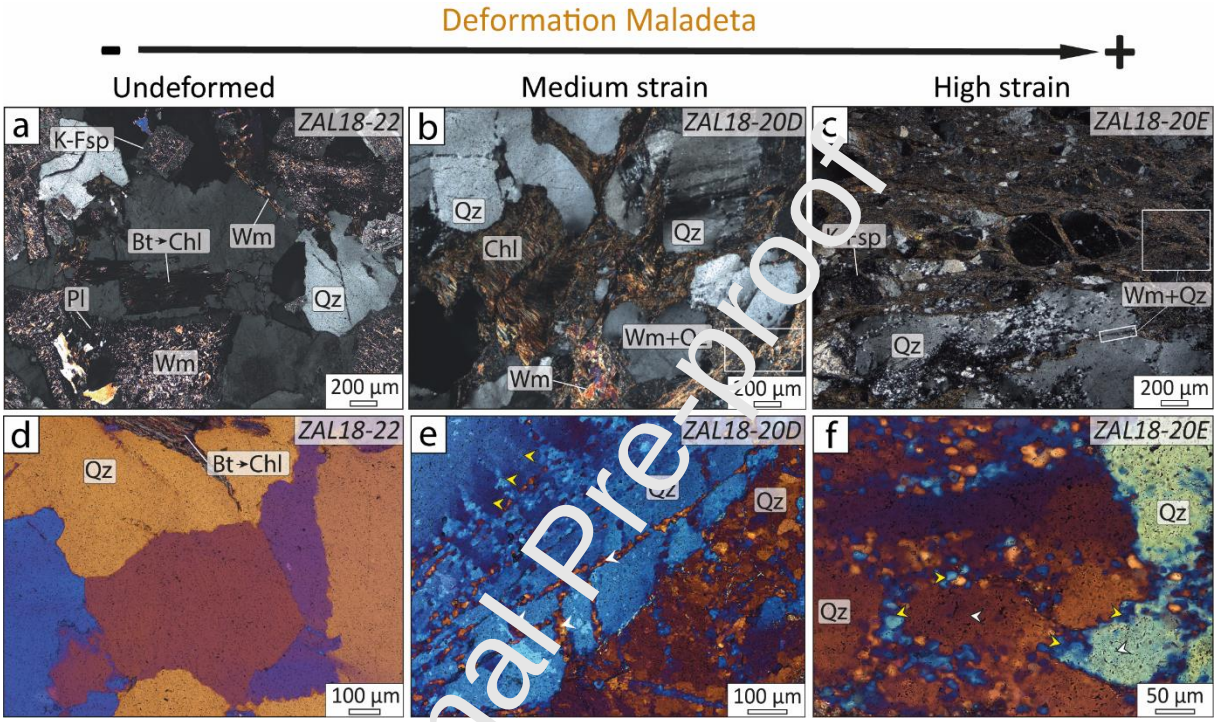

Figure 8 Microviews (high magnification) of samples in Maladeta transect, from undeformed granitoid (left) to high strain samples (right). Plane transmitted light image samples ZAL18-22, ZAL18-20D and ZAL18-20E, respectively. (d), (e) and (f) Microviews showing quartz recrystallisation and deformation features under cross-polarised light with lambda plate inserted for the same samples. SGR: subgrain rotation. White and yellow arrows, see main text.

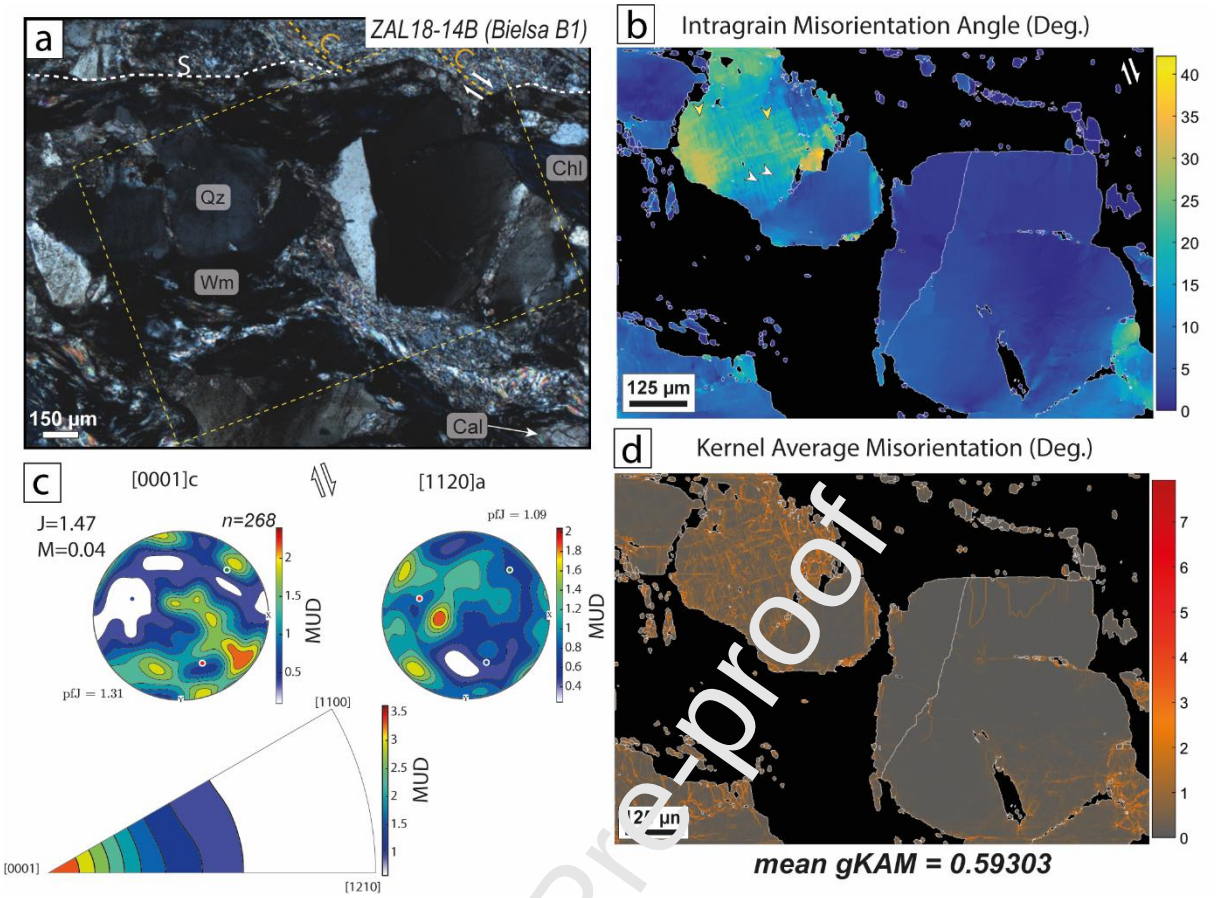

Figure 9: Electron Backscatter Diffraction (EBSD) results for sample ZAL18-14B (B1). (a) Microview of the analyzed area. (b) Map of intragrain misorientation angle. White arrows: narrow deformation bands (NDB). Yellow arrows: wide deformation bands (WDB). (c) Crystal preferred orientation (CPO) for all quartz grains (top) and inverse pole figure (bottom) with isocontours and color scale highlighting multiples of a uniform distribution (MUD). The IPF shows that lattice rotation axes across low-angle boundaries concentrate around the [0001]c, which suggests prism <a> slip as the dominant slip system for quartz plasticity. (d) Map of kernel average misorientation (KAM) angle.

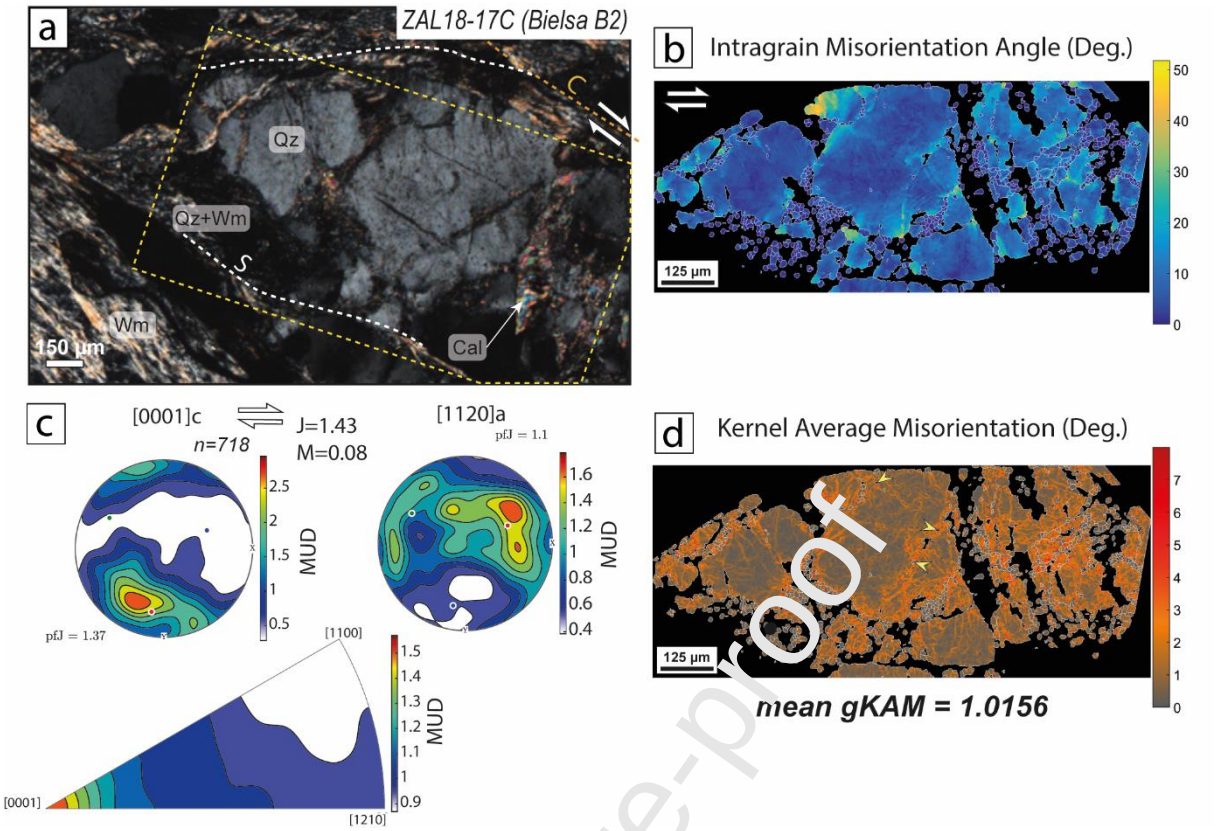

Figure 10 Electron Backscatter Diffraction (EBSD) results for sample ZAL18-17C (B2). (a) Microview of the analyzed area. (b) Map of intragrain misorientation angle. (c) Crystal preferred orientation (CPO) for all quartz grains (top) and inverse pole figure (bottom) collecting the distribution of misorientation axes across intra-grain (low-angle) boundaries. Their concentration around the [c] axis indicates dominant prism <a> dislocation slip system. (d) Maps of kernel average misorientation (KAM) angle. MUD = multiple of uniform distribution.

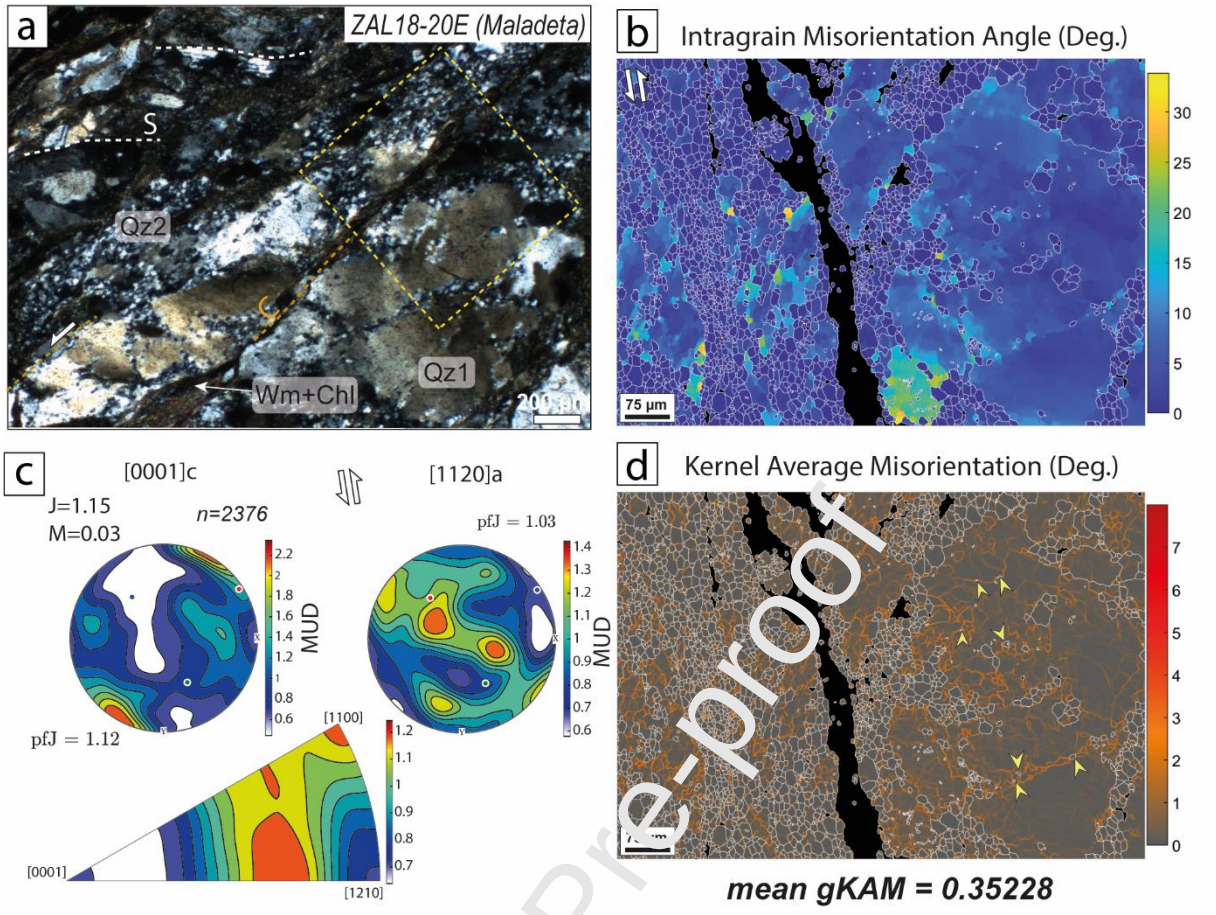

Figure 11 Electron Backscatter Diffraction (EBSD) results for sample ZAL18-20E (Maladeta). (a) Microview of the analyzed area. (b) Map of intragrain misorientation angle. (c) Quartz crystal preferred orientation (CPO) (top) and inverse pole figure (bottom) suggesting rhomb <a> and basal <a> slip systems to be dominant. (d) Map of kernel average misorientation (KAM) angle. Isocontours and color scale indicate multiples of a uniform distribution (MUD).

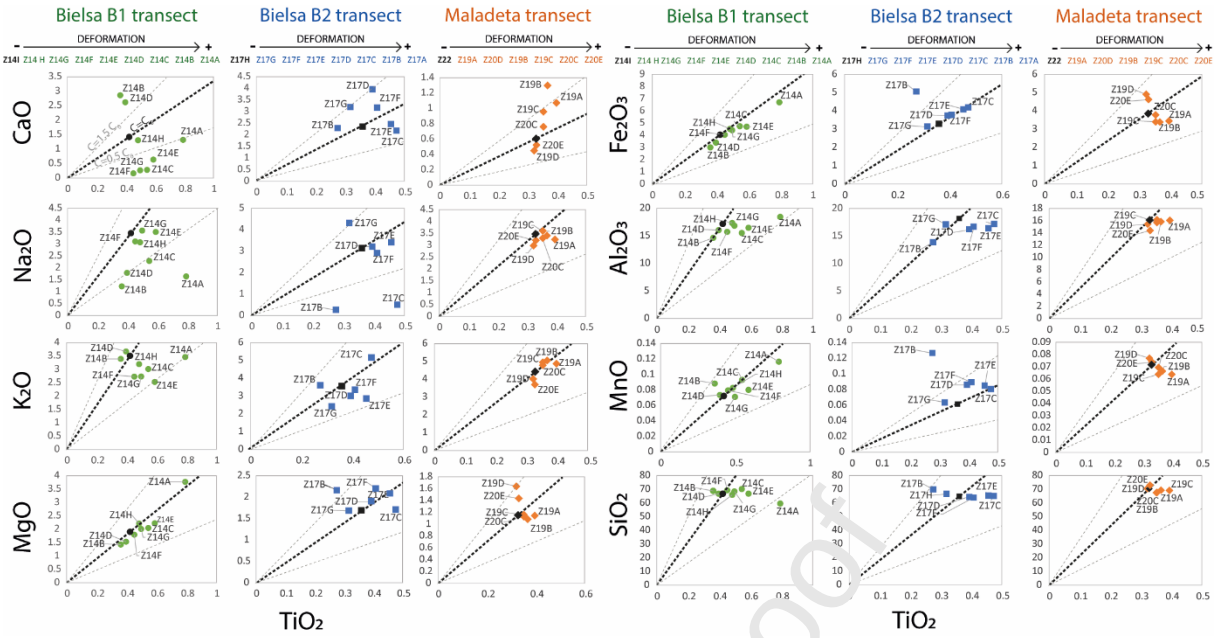

Figure 12 Major elemental variations in transects B1, B2 and Maladeta. Each major element content is plotted as a function of the TiO_2 content (see text for details). Black dot: composition of undeformed sample in each transect. Black dashed line $C=C_0$: constant isocon (Grant, 1986) constructed from the chemical composition of undeformed sample (C_0) of each transect. The grey dashed line $C=1.5C_0$ above the black isocon represents 50% gain in the element *x* relative to the undeformed sample (C_0). The grey dashed line $C=0.5C_0$ below the black isocon represents 50% loss in the element *x* relative to the undeformed sample (C_0). Sample names are shortened (e.g. ZAL18-14B to Z14B).

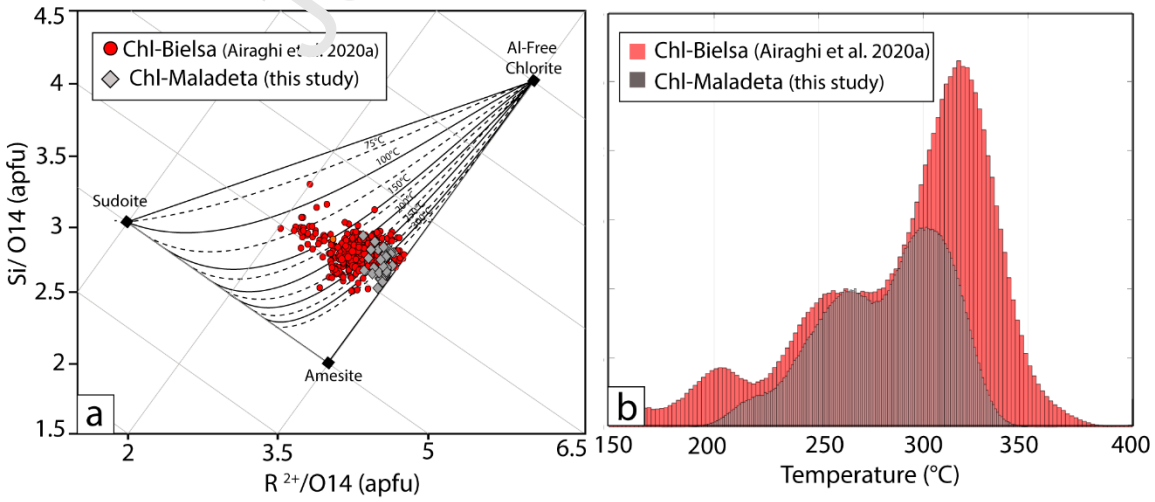

Figure 13 Temperature ranges estimated from chlorite thermometry. Grey: Temperature from Maladeta chlorites. Red: Temperatures available for Bielsa chlorites (Airaghi et al., 2020a). (a) Temperatures obtained with the thermometer of Bourdelle et al. (2013) in its graphical form (Bourdelle and Cathelineau, 2015). (b) Temperature range obtained with the thermometer of Vidal et al. (2006) tested with a Montecarlo simulation (3000 iterations), with estimated 20-30% Fe^{3+} (from iterative calculations).

	Sample	J	M	gKAM (°)	Qz1			Qz2		
					Grain-size (µm)	Average AR [σ]	IGM (°)	Grain-size (µm)	Average AR (σ)	IGM (°)
Bielsa B1	ZAL18-14B	1.47	0.04	0.59	> 50 µm	2.13 [1.33]	2-43	< 50 µm	1.98 [1.34]	0-18
	ZAL18-17B	1.65	0.12	0.59	> 50 µm	2.19 [0.69]	5-40	< 50 µm	1.72 [0.58]	0-14
Bielsa B2	ZAL18-17C	1.43	0.08	1.02	> 50 µm	2.28 [1.42]	6-50	< 50 µm	1.61 [0.51]	0-19
	ZAL18-17C	1.06	0.02	0.69	> 50 µm	-	-	< 50 µm	1.57 [0.46]	0-18
Maladeta	ZAL18-20C	1.53	0.06	0.29	25.94 ± 0.64*	1.74 ± 0.48	7-40	11.88 ± 0.47	1.39 ± 0.27	0-11
	ZAL18-20E	1.15	0.03	0.35	16.90 ± 0.70*	1.73 ± 0.48	5-33	9.00 ± 0.54	1.44 ± 0.33	0-12

Table 1 Crystallographic characteristics of quartz in studied samples. gKAM: grain Kernel Average Misorientation. AR: Aspect Ratio. IGM: Intragranular Misorientation range.

	Sam-ple	J	M	gKAM (°)	Qz1			Qz2		
					Grain-size (µm)	Aver-age AR [σ]	IGM (°)	Grain-size (µm)	Aver-age AR (σ)	IGM (°)
Bielsa B1	ZAL18-14B	1.47	0.04	0.59	> 50 µm	2.13 [1.33]	2-43	< 50 µm	1.98 [1.34]	0-18
	ZAL18-17B	1.65	0.12	0.59	> 50 µm	2.19 [0.69]	5-40	< 50 µm	1.72 [0.58]	0-14
Bielsa B2	ZAL18-17C	1.43	0.08	1.02	> 50 µm	2.28 [1.42]	6-50	< 50 µm	1.61 [0.51]	0-19
	ZAL18-17C	1.06	0.02	0.69	> 50 µm	-	-	< 50 µm	1.57 [0.46]	0-18
Mal-a-deta	ZAL18-20C	1.53	0.06	0.29	25.94 ± 0.64*	1.74 ± 0.48	7-40	11.88 ± 0.47	1.39 ± 0.27	0-11
	ZAL18-20E	1.15	0.03	0.35	16.90 ± 0.70*	1.73 ± 0.48	5-33	9.00 ± 0.54	1.44 ± 0.33	0-12

* Qz1 (parent grains) and Qz2 (recrystallized grains) are classified according the GOS criteria ()

Table 2 Major element whole-rock composition (in wt %) for all analyzed samples. The total weight % of oxides (with LOI values added) is in the range of 99-103 %, consistent with the uncertainty of the LOI analytical technique (100 ± 1.0 %). Relative elemental gain/loss in calculated in % compared to least deformed sample of each transect, relative to immobile Ti. Grey areas identify samples in B2 whose bulk rock is not in the suite of the transect (see text for details).

		Bulk rock composition (wt %)													Relative gain/loss with respect to immobile Ti (%)							
	Sample	SiO_2	TiO_2	Al_2O_3	Cr_2O_3	Fe_2O_3	MnO	MgO	CaO	Na_2O	K_2O	P_2O_5	L.O.I.	TOTAL	SiO_2	TiO_2	Al_2O_3	Fe_2O_3	MgO	CaO	Na_2O	K_2O
Bielsa 1	ZAL18-14A	59.58	0.79	18.45	0.01	6.70	0.12	3.77	1.32	1.64	3.46	0.16	4.78	100.47	-52.24	0.00	-42.59	-11.36	5.89	-50.36	-74.63	-47.22
	ZAL18-14B	68.78	0.36	14.63	0.00	3.01	0.09	1.43	2.82	1.22	3.39	0.10	4.67	100.56	-20.62	0.00	-0.36	-13.07	-12.23	-13.58	-58.60	-13.21
	ZAL18-14C	70.17	0.55	15.52	0.00	4.75	0.09	2.05	2.28	2.29	3.01	0.15	2.87	101.75	-18.34	0.00	-29.87	-8.90	-16.48	-84.50	-48.62	-33.30
	ZAL18-14D	66.73	0.40	16.05	0.00	4.00	0.07	1.54	2.62	1.79	3.67	0.12	4.53	100.91	-6.72	0.00	-0.36	-10.42	-14.03	96.95	-44.85	11.66
	ZAL18-14E	66.76	0.59	16.47	0.00	4.70	0.08	2.22	0.64	3.51	2.53	0.17	2.91	100.57	-27.99	0.00	-31.04	-16.41	-15.98	-67.71	-27.03	-48.04
	ZAL18-	69.	0.	15.	0.	4.	0.	1.	0.	3.	2.	0.	2.	100.	-2.	0.	-14	-6.	-11.	-89.	-15	-27

	14F	31	45	73	000	004	008	080	166	111	773	133	666	**211**	61	00	.200	35	58	28	.74	.05
	ZAL18-14G	68.42	0.50	16.84	0.000	4.042	0.007	2.001	0.026	3.057	2.774	0.015	2.665	**1016.63**	-12.76	00	-16.63	-7.08	-10.18	-84.20	-12.35	-33.64
	ZAL18-14H	65.90	0.48	17.34	0.000	4.052	0.008	2.211	1.311	3.307	3.200	0.115	3.388	**1016.64**	-13.57	00	-11.72	-2.17	1.665	-19.39	-22.32	-20.25
	ZAL18-14I	66.71	0.42	17.18	0.000	4.004	0.007	1.911	1.422	3.466	3.511	0.113	2.298	**1016.12**	0.000	00	0.000	0.000	0.000	0.000	0.000	0.000
Bielsa 2	**ZAL18-17A**	77.91	0.21	9.94	0.000	5.083	0.008	2.466	0.366	0.211	2.201	0.110	2.187	**1019.98**	111.04	00	-3.97	21 2.24	155.87	-73.37	-88.21	-0.91
	ZAL18-17B	69.95	0.27	13.87	0.000	5.003	0.013	2.117	2.131	0.326	3.361	0.110	4.186	**1022.56**	41.74	00	0.200	10 1.69	68.54	27.56	-89.26	32.88
	ZAL18-17C	65.33	0.47	17.11	0.000	4.019	0.008	1.170	2.220	0.500	5.116	0.112	4.153	**1014.40**	-23.35	00	-28.42	-2.74	-23.35	-29.62	-87.99	9.811
	ZAL18-17D	64.61	0.39	16.12	0.000	3.073	0.009	1.990	3.999	3.320	2.999	0.111	4.165	**1017.79**	-8.49	00	-18.58	4.457	3.301	54.02	-6.54	-23.02
	ZAL18-17E	65.11	0.46	16.29	0.000	4.008	0.008	2.077	2.488	3.403	2.855	0.133	3.545	**1005.11**	-20.38	00	-28.95	-1.24	-2.777	-17.19	-14.18	-36.72

	ZAL18-17F	64.02	0.41	16.61	0.00	3.78	0.09	2.20	3.19	2.91	3.38	0.11	4.49	**1012.20**	-12.79	0.00	-19.30	1.73	15.05	18.62	-18.21	-16.42
	ZAL18-17G	66.57	0.32	17.04	0.00	3.12	0.06	1.68	3.22	4.31	2.43	0.10	3.50	**1022.36**	16.49	0.00	6.33	7.97	12.69	53.50	-55.56	-22.75
	ZAL18-17H	64.64	0.36	18.13	0.00	3.27	0.06	1.69	2.37	3.14	3.56	0.11	4.77	**1022.10**	0.00	0.00	0.00	0.00	0.00	0.00	0.00	0.00
Maladeta	**ZAL18-20E**	72.53	0.33	14.38	0.00	4.61	0.07	1.43	0.52	3.19	3.70	0.10	1.64	**1012.55**	2.38	0.00	-11.23	18.81	23.54	-15.68	-7.91	-16.26
	ZAL18-20C	67.66	0.35	16.20	0.00	3.80	0.07	1.13	0.76	3.28	4.75	0.17	1.03	**999.21**	-10.75	0.00	-6.53	-8.52	-8.94	16.54	-11.45	0.65
	ZAL18-19C	67.49	0.35	15.73	0.00	3.40	0.06	1.15	0.96	3.58	4.92	0.17	1.48	**999.31**	-10.99	0.00	-9.25	-18.03	-7.17	46.00	-3.38	4.08
	ZAL18-19B	69.31	0.37	15.87	0.00	3.39	0.07	1.09	1.29	3.39	5.07	0.19	1.50	**1012.55**	-12.02	0.00	-11.86	-21.30	-15.28	90.06	-12.03	3.40
	ZAL18-20D	70.80	0.32	15.45	0.00	4.90	0.08	1.64	0.45	2.98	4.00	0.17	1.96	**1022.74**	2.38	0.00	-2.31	29.40	44.51	-25.50	-11.94	-7.11
	ZAL18-	69.	0.40	16.	0.00	3.45	0.06	1.15	1.07	3.23	4.89	0.17	1.57	**1012.**	-18.	0.00	-17.	-25.	-17.	45.56	-22.	-7.

	19A	46		11										**56**	43		25	90	88		49	71
	ZAL18-22	70.62	0.33	16.14	0.000	3.887	0.07	1.16	0.61	3.45	4.40	0.17	1.69	**102.50**	0.00	0.00	0.00	0.00	0.00	0.00	0.00	0.00	0.00	0.00

Credit author statement

Khadija Alaoui : Conceptualization, Writing, Original Draft, Investigation, Formal analysis, Visualization
Laura Airaghi : Conceptualization, Investigation, Formal analysis , Writing, Review and Editing
Benoit Dubacq : Conceptualization, Formal analysis, Writing, Review and Editing
Claudio L. Rosenberg : Conceptualization, Supervision, validation
Nicolas Bellahsen : Supervision, validation, Founding acquisition
Jacques Précigout : Formal analysis, validation, Writing, Review and Editing

Declaration of interests

☒The authors declare that they have no known competing financial interests or personal relationships that could have appeared to influence the work reported in this paper.

☐The authors declare the following financial interests/personal relationships which may be considered as potential competing interests:

Highlights :

- Deformation is localized only in granite showing weak pre-kinematic alteration
- Direct transition from fracturing to subgrain rotation in quartz occurs at T<370°C
- Pre-shearing fluid-rock interaction promotes phyllosilicate growth and phase mixing
- Pre-conditioning of protolith controls the (micro)structural style in low-T shear zones

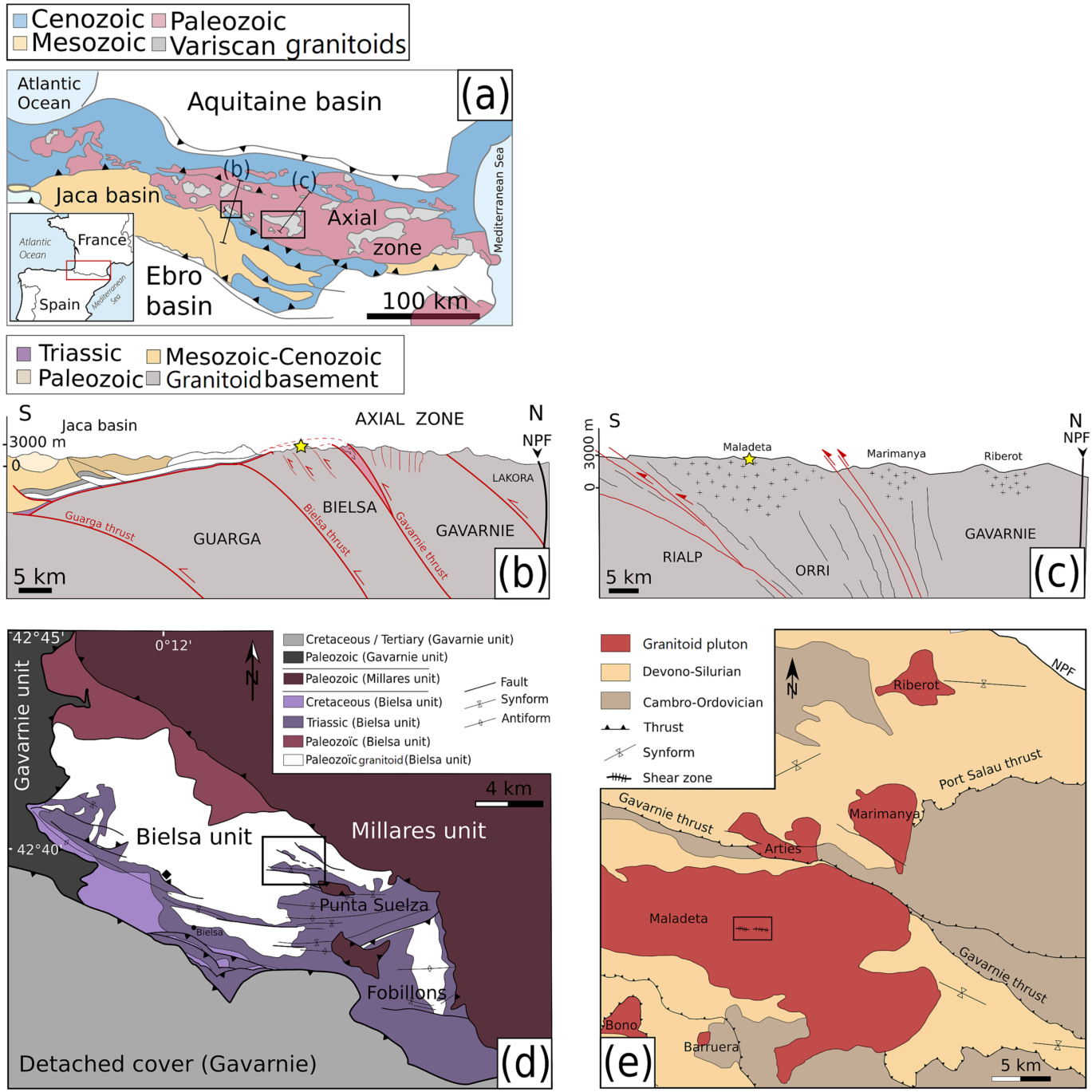
Cenozoic
Paleozoic
Mesozoic
Variscan granitoids
Atlantic Ocean
Aquitaine basin
(a)
(b)
(c)
Jaca basin
Axial zone
Mediterranean Sea
France
Spain
Ebro basin
100 km
Triassic
Mesozoic-Cenozoic
Paleozoic
Granitoid basement
S
N
Jaca basin
AXIAL ZONE
3000 m
0
NPF
LAKORA
BIELSA
Guarga thrust
Bielsa thrust
Gavarnie thrust
GUARGA
GAVARNIE
5 km
(b)
Maladeta
Marimanya
Riberot
RIALP
ORRI
(c)
42°45'
0°12'
42°40'
Gavarnie unit
Cretaceous / Tertiary (Gavarnie unit)
Paleozoic (Gavarnie unit)
Paleozoic (Millares unit)
Cretaceous (Bielsa unit)
Triassic (Bielsa unit)
Paleozoïc (Bielsa unit)
Paleozoïc granitoid (Bielsa unit)
Fault
Synform
Antiform
4 km
Bielsa unit
Millares unit
Punta Suelza
Bielsa
Fobillons
Detached cover (Gavarnie)
(d)
Granitoid pluton
Devono-Silurian
Cambro-Ordovician
Thrust
Synform
Shear zone
NPF
Riberot
Port Salau thrust
Gavarnie thrust
Marimanya
Arties
Maladeta
Gavarnie thrust
Bono
Barruera
5 km
(e)

Figure 1

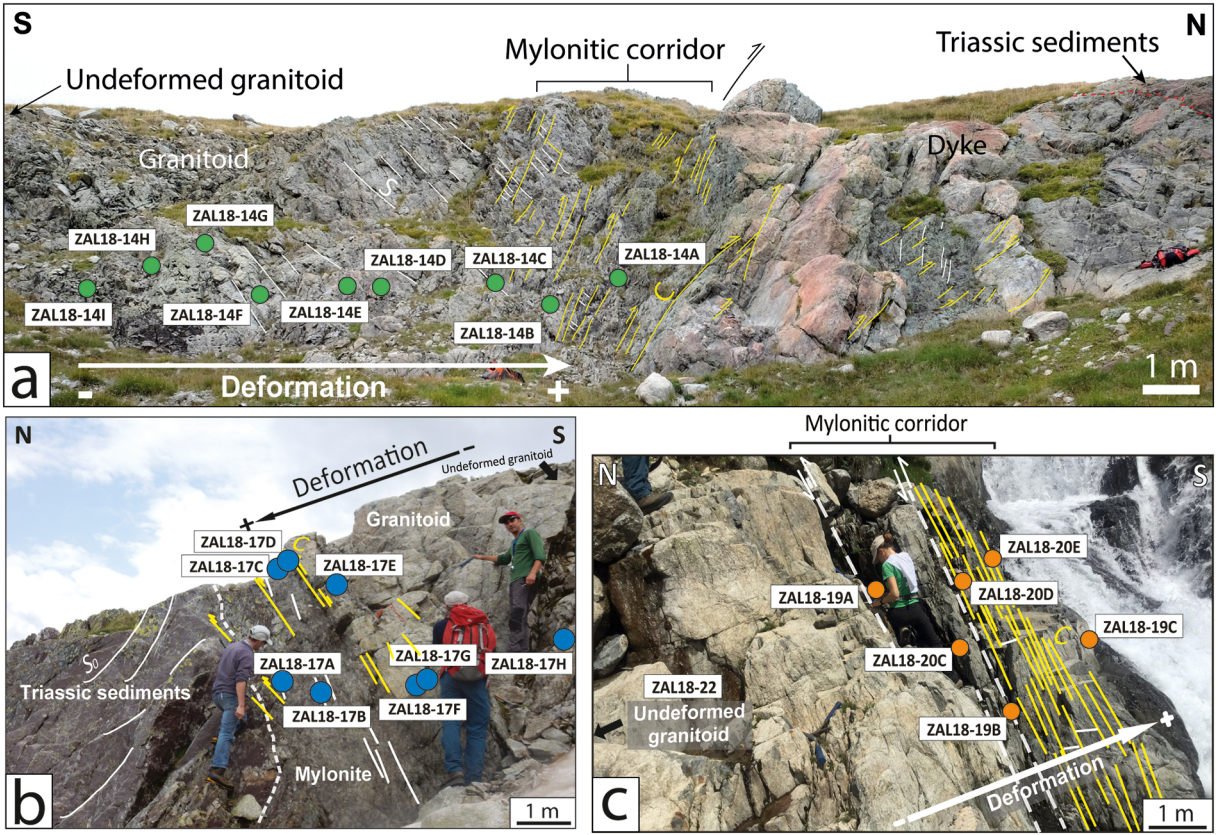
S
N
Undeformed granitoid
Mylonitic corridor
Triassic sediments
Granitoid
Dyke
ZAL18-14G
ZAL18-14H
ZAL18-14D
ZAL18-14C
ZAL18-14A
ZAL18-14I
ZAL18-14F
ZAL18-14E
ZAL18-14B
a
Deformation
1 m
N
S
Deformation
Undeformed granitoid
Granitoid
ZAL18-17D
ZAL18-17C
ZAL18-17E
ZAL18-17A
ZAL18-17G
ZAL18-17H
ZAL18-17B
ZAL18-17F
Triassic sediments
Mylonite
b
1 m
Mylonitic corridor
N
S
ZAL18-20E
ZAL18-19A
ZAL18-20D
ZAL18-19C
ZAL18-20C
ZAL18-22
Undeformed granitoid
ZAL18-19B
Deformation
C
1 m

Figure 2

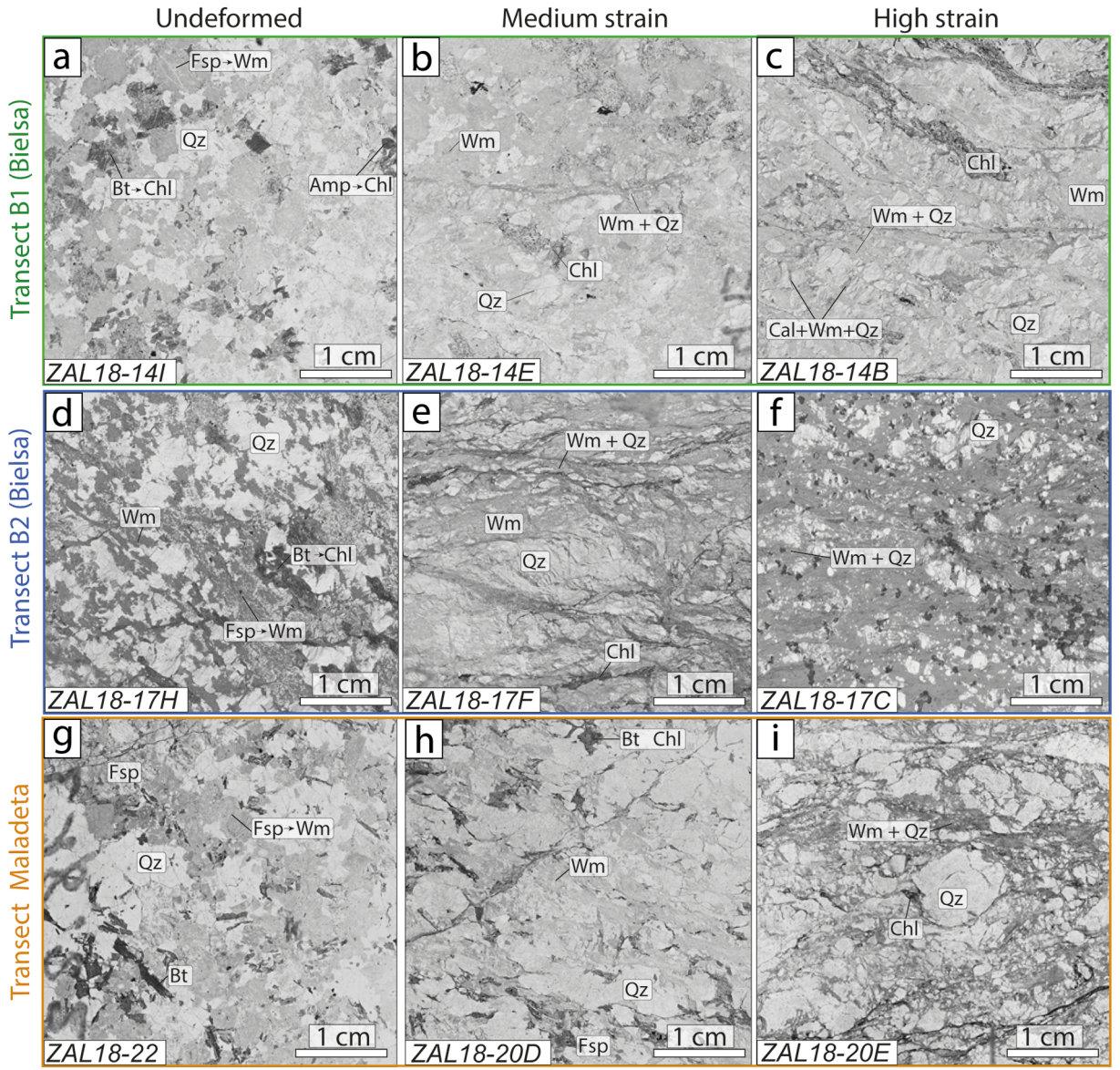
Undeformed
Medium strain
High strain
Transect B1 (Bielsa)
Transect B2 (Bielsa)
Transect Maladeta
a
Fsp→Wm
Qz
Bt→Chl
Amp→Chl
ZAL18-14I
1 cm
b
Wm
Wm + Qz
Chl
Qz
ZAL18-14E
1 cm
c
Chl
Wm
Wm + Qz
Cal+Wm+Qz
Qz
ZAL18-14B
1 cm
d
Qz
Wm
Bt→Chl
Fsp→Wm
ZAL18-17H
1 cm
e
Wm + Qz
Wm
Qz
Chl
ZAL18-17F
1 cm
f
Qz
Wm + Qz
ZAL18-17C
1 cm
g
Fsp
Fsp→Wm
Qz
Bt
ZAL18-22
1 cm
h
Bt Chl
Wm
Qz
Fsp
ZAL18-20D
1 cm
i
Wm + Qz
Qz
Chl
ZAL18-20E
1 cm

Figure 3

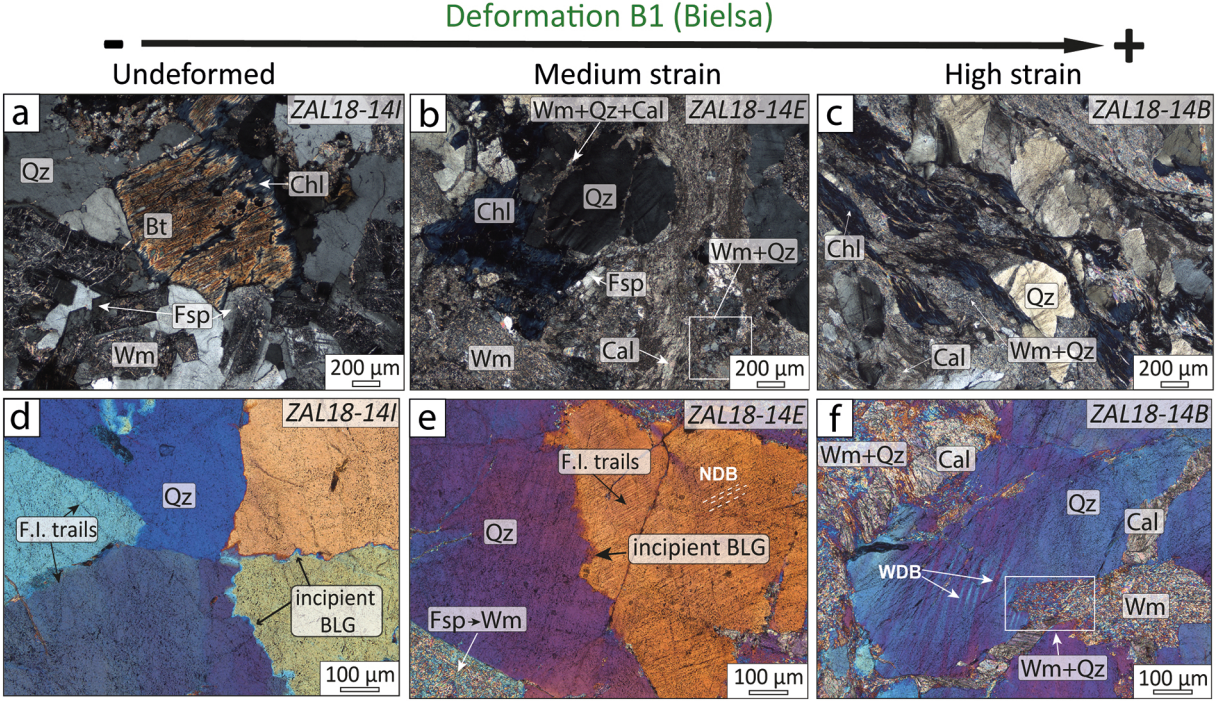
Deformation B1 (Bielsa)
-
+
Undeformed
Medium strain
High strain
a
ZAL18-14I
Qz
Chl
Bt
Fsp
Wm
200 µm
b
Wm+Qz+Cal
ZAL18-14E
Chl
Qz
Wm+Qz
Fsp
Wm
Cal
200 µm
c
ZAL18-14B
Chl
Qz
Cal
Wm+Qz
200 µm
d
ZAL18-14I
Qz
F.I. trails
incipient BLG
100 µm
e
ZAL18-14E
F.I. trails
NDB
Qz
incipient BLG
Fsp→Wm
100 µm
f
ZAL18-14B
Wm+Qz
Cal
Qz
Cal
WDB
Wm
Wm+Qz
100 µm

Figure 4

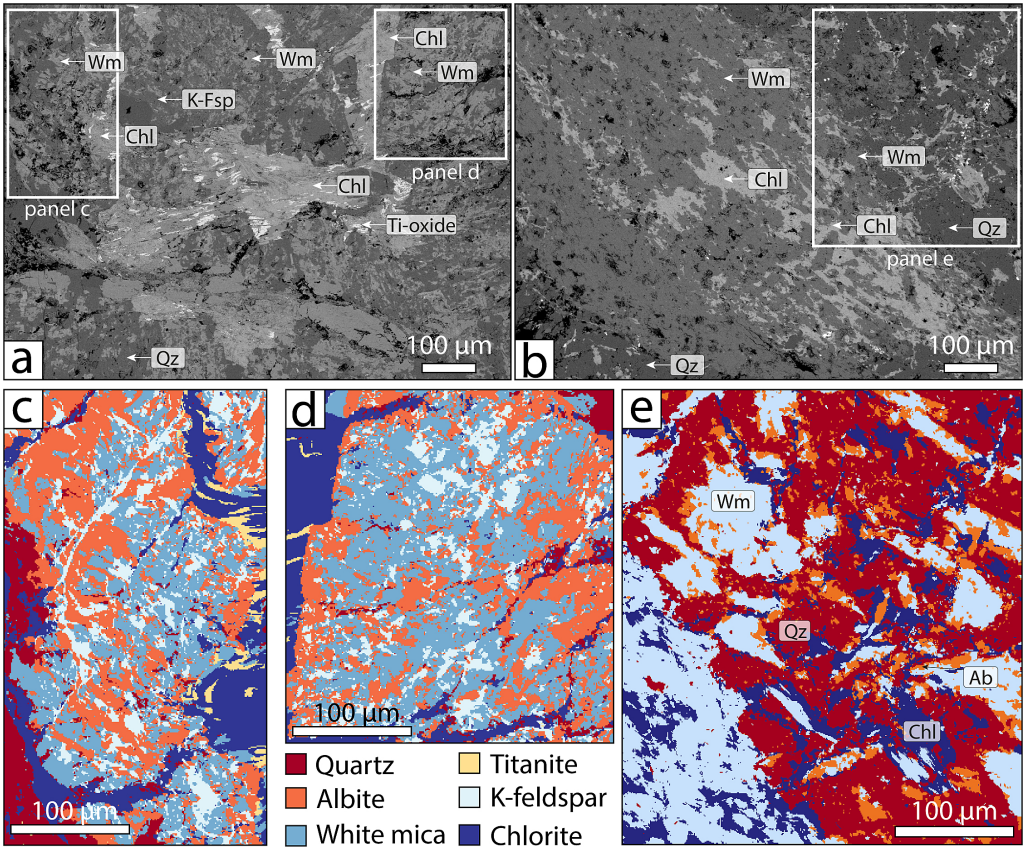
a
Wm
Wm
K-Fsp
Chl
Chl
Ti-oxide
Qz
100 µm
panel c
Chl
Wm
panel d
b
Wm
Chl
Qz
100 µm
Wm
Chl
Qz
panel e
c
100 µm
d
100 µm
e
Wm
Qz
Ab
Chl
100 µm
Quartz
Albite
White mica
Titanite
K-feldspar
Chlorite

Figure 5

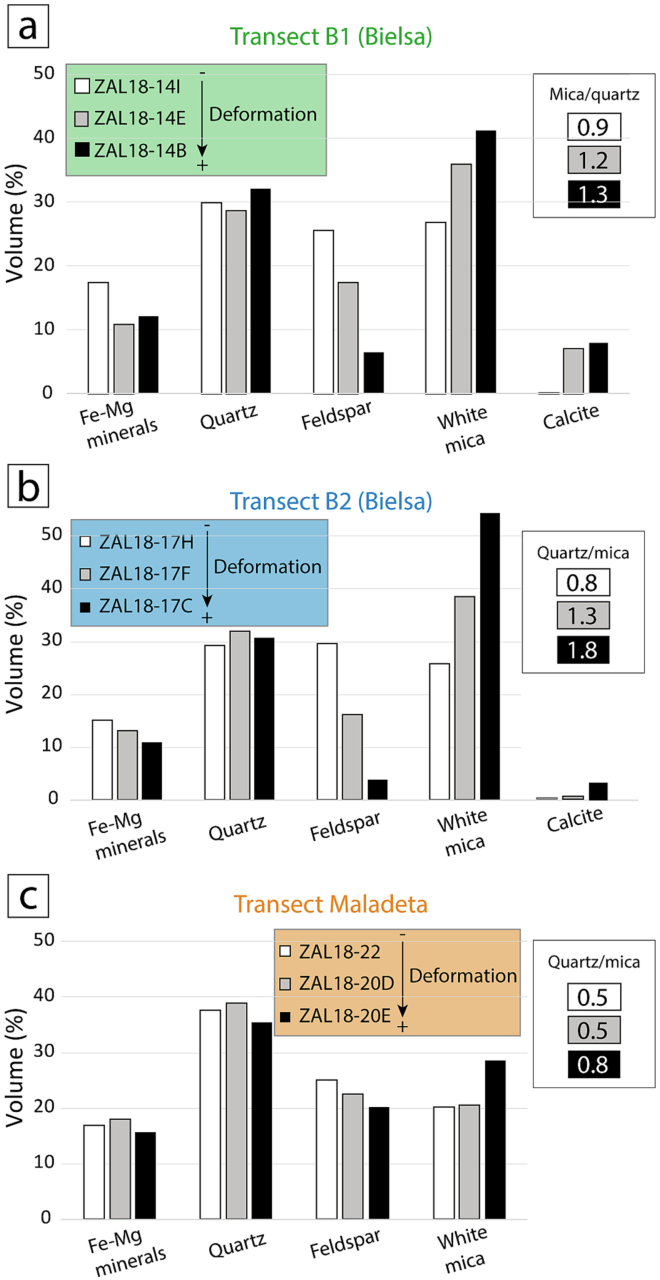
a
Transect B1 (Bielsa)
ZAL18-14I
ZAL18-14E
ZAL18-14B
Deformation
-
+
Mica/quartz
0.9
1.2
1.3
Volume (%)
50
40
30
20
10
0
Fe-Mg minerals
Quartz
Feldspar
White mica
Calcite
b
Transect B2 (Bielsa)
ZAL18-17H
ZAL18-17F
ZAL18-17C
Deformation
Quartz/mica
0.8
1.3
1.8
Volume (%)
Fe-Mg minerals
Quartz
Feldspar
White mica
Calcite
c
Transect Maladeta
ZAL18-22
ZAL18-20D
ZAL18-20E
Deformation
Quartz/mica
0.5
0.5
0.8
Volume (%)
Fe-Mg minerals
Quartz
Feldspar
White mica

Figure 6

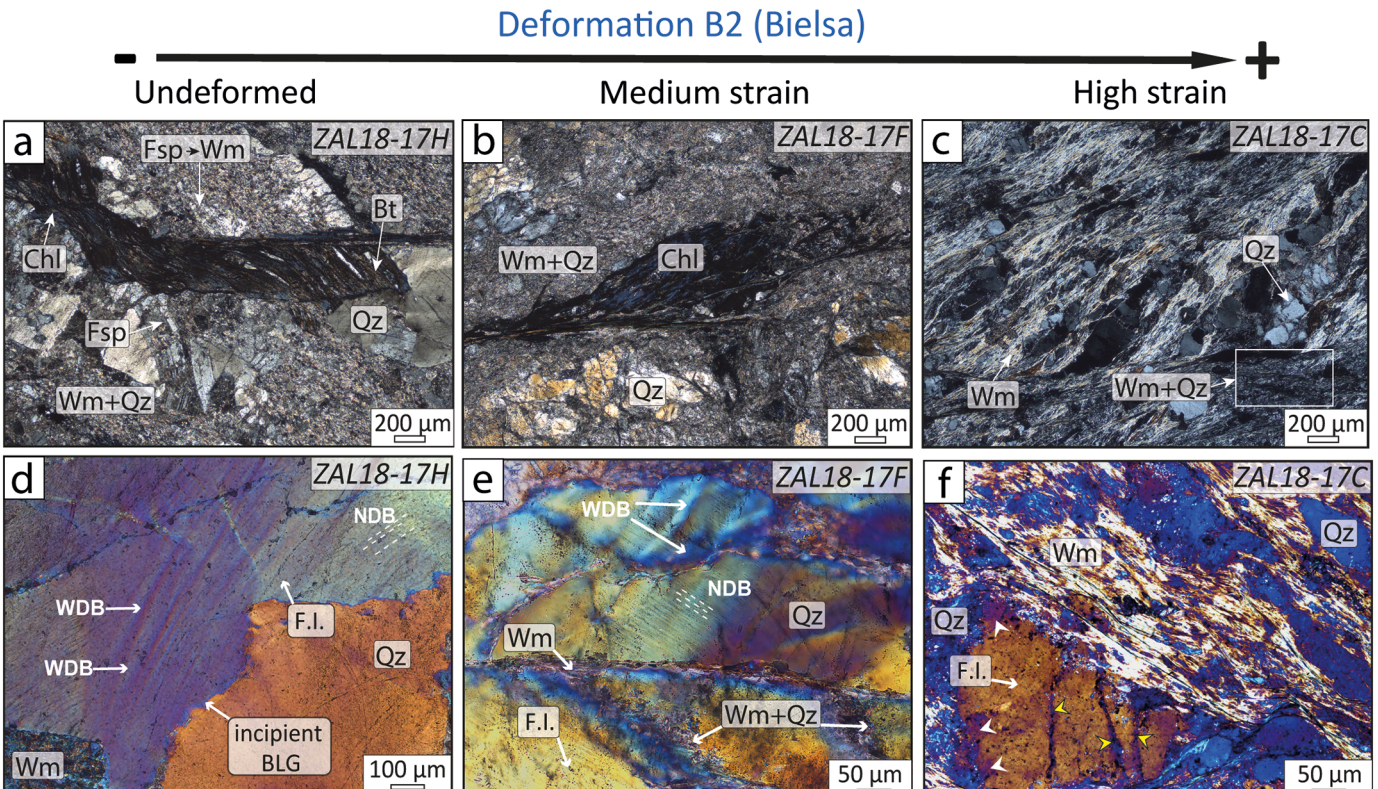
Deformation B2 (Bielsa)
-
+
Undeformed
Medium strain
High strain
a
ZAL18-17H
Fsp→Wm
Bt
Chl
Fsp
Qz
Wm+Qz
200 µm
b
ZAL18-17F
Wm+Qz
Chl
Qz
200 µm
c
ZAL18-17C
Qz
Wm
Wm+Qz
200 µm
d
ZAL18-17H
NDB
WDB
WDB
F.I.
Qz
incipient BLG
Wm
100 µm
e
ZAL18-17F
WDB
NDB
Qz
Wm
F.I.
Wm+Qz
50 µm
f
ZAL18-17C
Qz
Wm
Qz
F.I.
50 µm

Figure 7

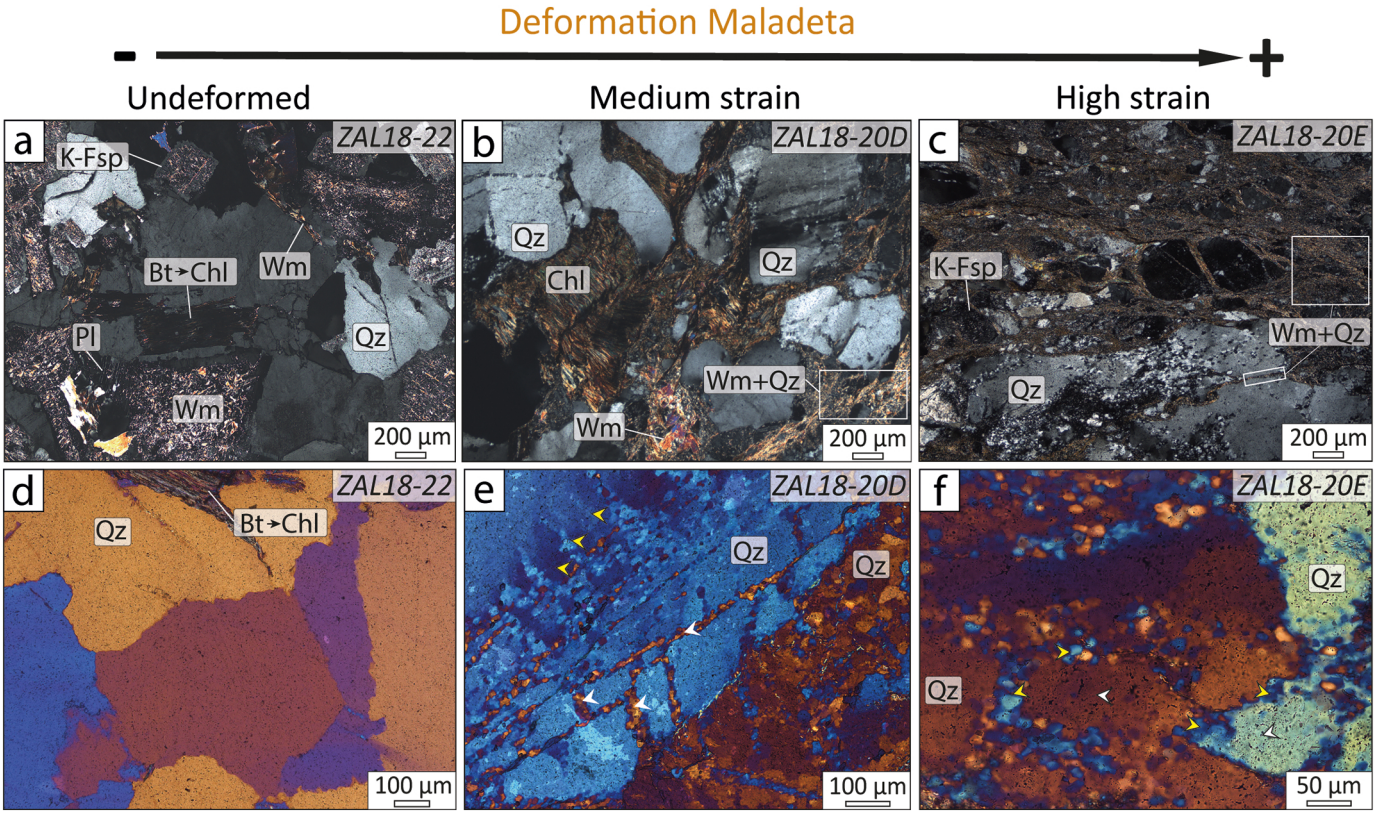
Deformation Maladeta
-
+
Undeformed
Medium strain
High strain
a
ZAL18-22
K-Fsp
Bt→Chl
Wm
Pl
Qz
Wm
200 µm
b
ZAL18-20D
Qz
Chl
Qz
Wm+Qz
Wm
200 µm
c
ZAL18-20E
K-Fsp
Wm+Qz
Qz
200 µm
d
ZAL18-22
Qz
Bt→Chl
100 µm
e
ZAL18-20D
Qz
Qz
100 µm
f
ZAL18-20E
Qz
Qz
50 µm

Figure 8

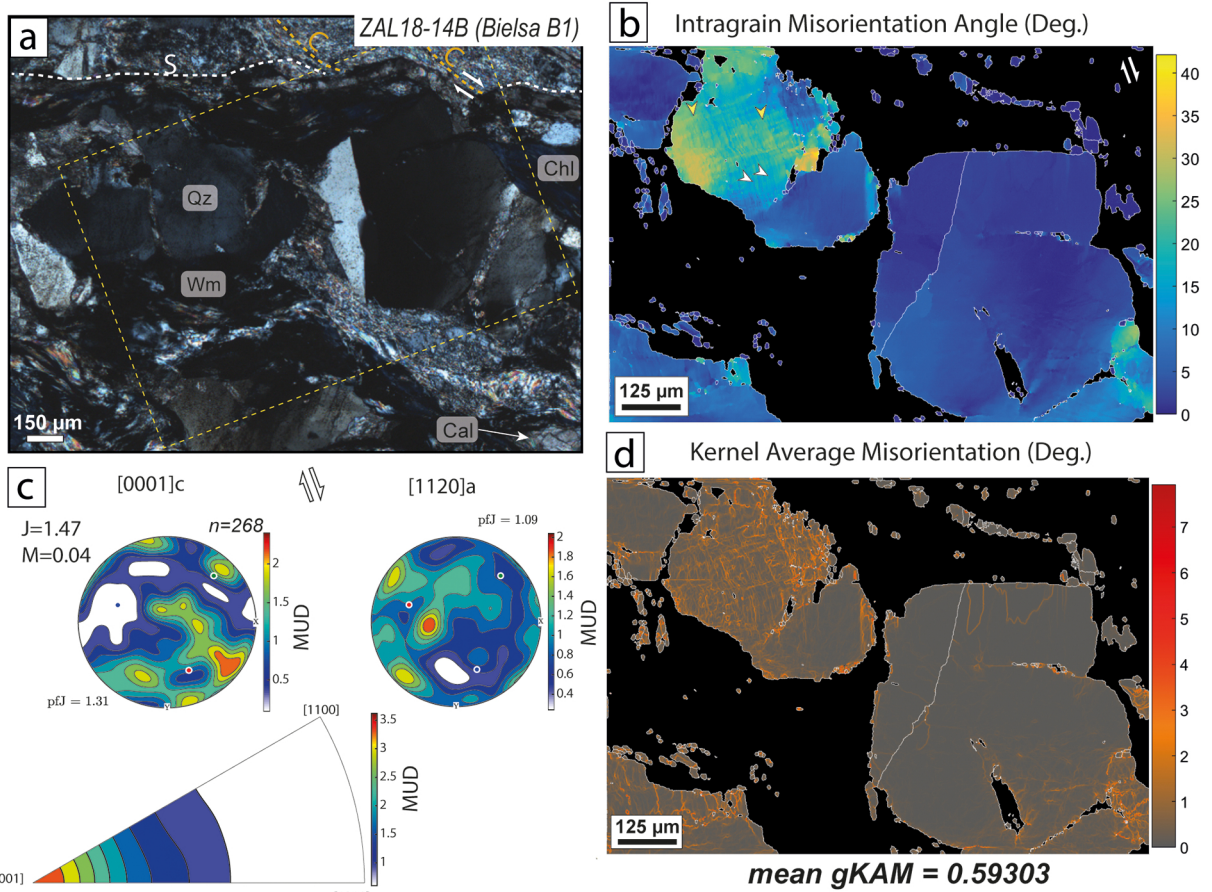
a
ZAL18-14B (Bielsa B1)
S
C
C
Chl
Qz
Wm
Cal
150 µm
b
Intragrain Misorientation Angle (Deg.)
40
35
30
25
20
15
10
5
0
125 µm
c
[0001]c
[1120]a
J=1.47
M=0.04
n=268
pfJ = 1.31
pfJ = 1.09
MUD
[1100]
[0001]
[1210]
d
Kernel Average Misorientation (Deg.)
7
6
5
4
3
2
1
0
125 µm
mean gKAM = 0.59303

Figure 9

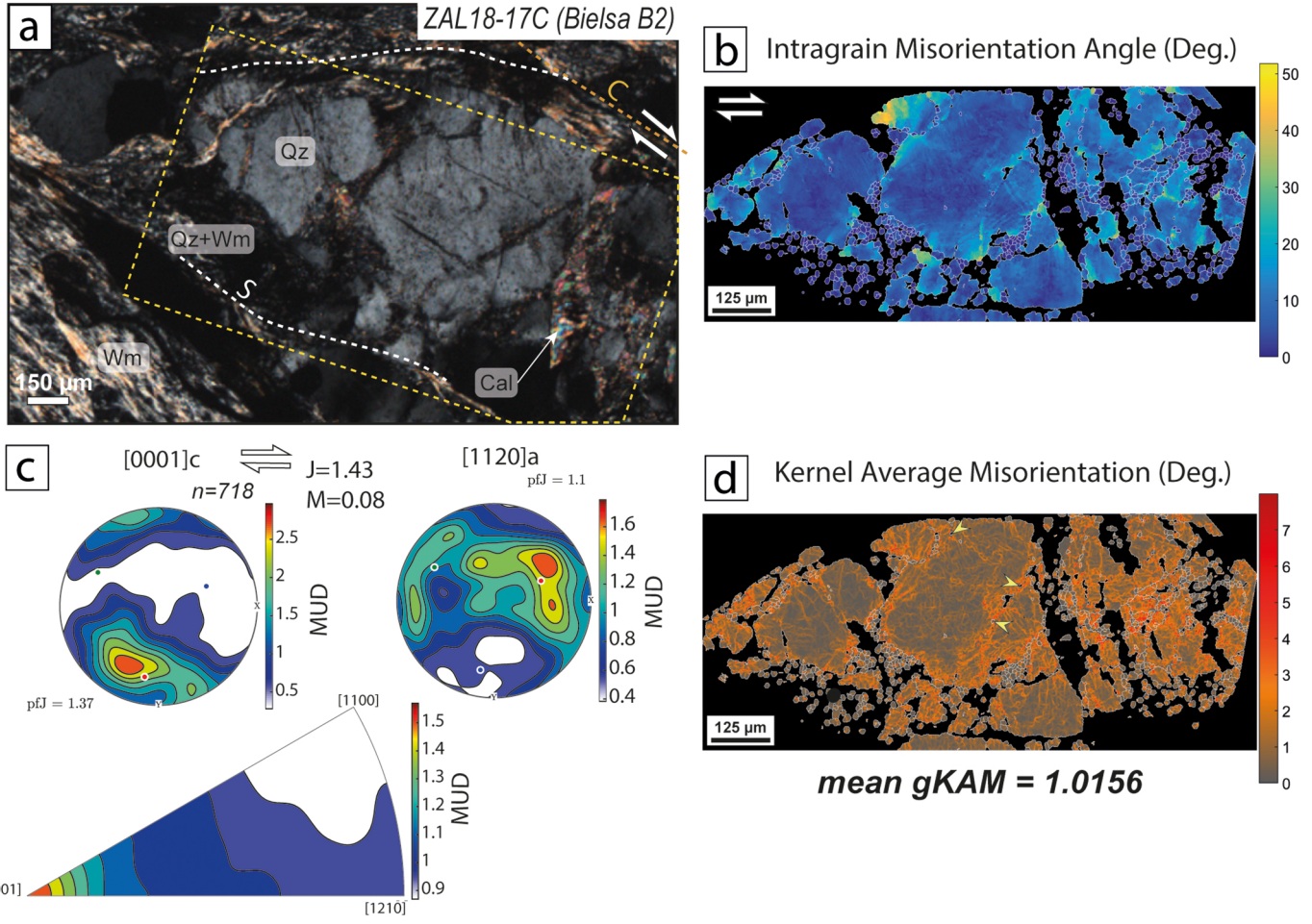
a
ZAL18-17C (Bielsa B2)
C
Qz
Qz+Wm
S
Wm
Cal
150 µm
b
Intragrain Misorientation Angle (Deg.)
125 µm
50
40
30
20
10
0
c
[0001]c
n=718
J=1.43
M=0.08
[1120]a
pfJ = 1.1
pfJ = 1.37
MUD
2.5
2
1.5
1
0.5
1.6
1.4
1.2
1
0.8
0.6
0.4
[1100]
[0001]
[1210]
1.5
1.4
1.3
1.2
1.1
1
0.9
d
Kernel Average Misorientation (Deg.)
125 µm
mean gKAM = 1.0156
7
6
5
4
3
2
1
0

Figure 10

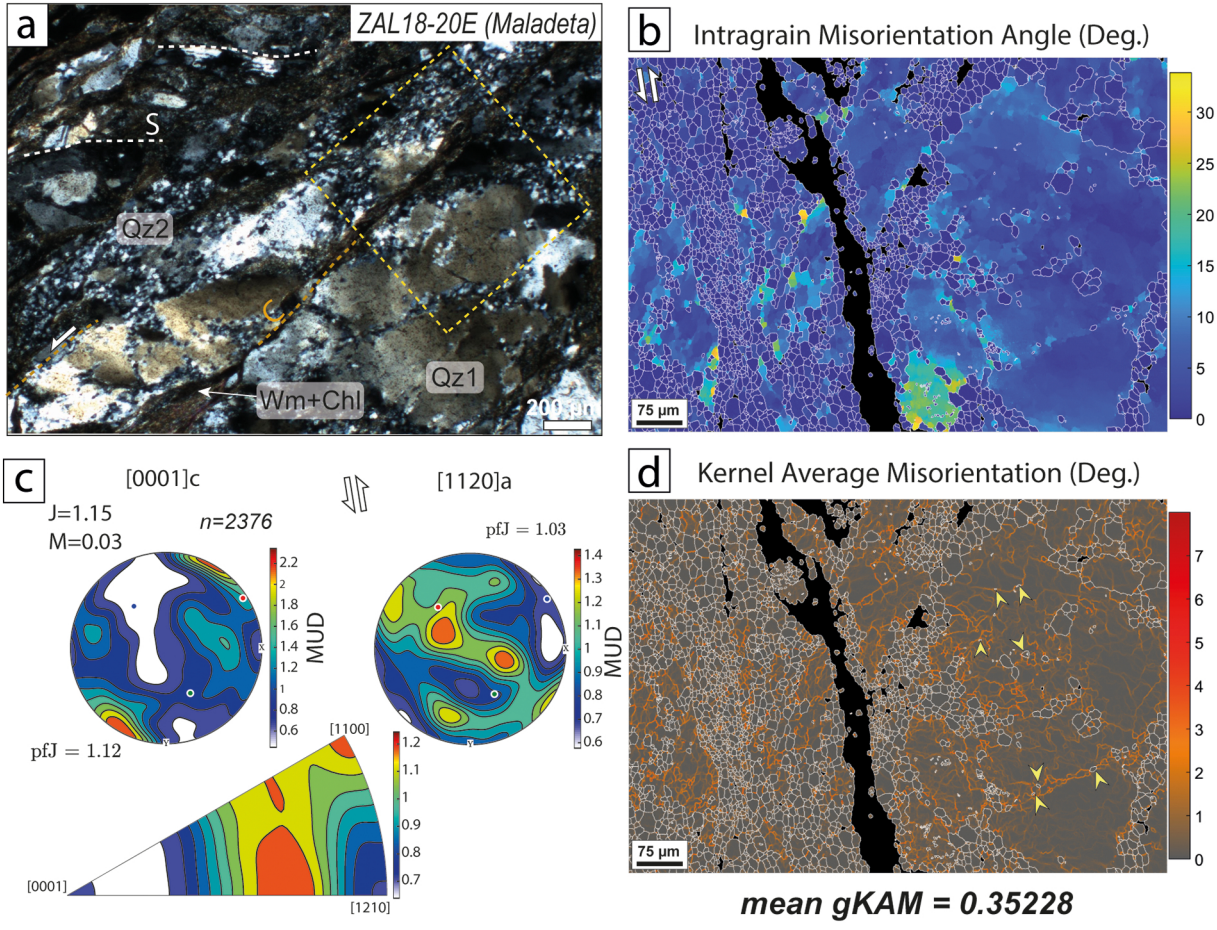
a
ZAL18-20E (Maladeta)
S
Qz2
C
Qz1
Wm+Chl
200 µm
b
Intragrain Misorientation Angle (Deg.)
30
25
20
15
10
5
0
75 µm
c
[0001]c
[1120]a
J=1.15
M=0.03
n=2376
pfJ = 1.03
MUD
2.2
2
1.8
1.6
1.4
1.2
1
0.8
0.6
1.4
1.3
1.2
1.1
1
0.9
0.8
0.7
0.6
pfJ = 1.12
[1100]
[0001]
[1210]
1.2
1.1
1
0.9
0.8
0.7
d
Kernel Average Misorientation (Deg.)
7
6
5
4
3
2
1
0
75 µm
mean gKAM = 0.35228

Figure 11

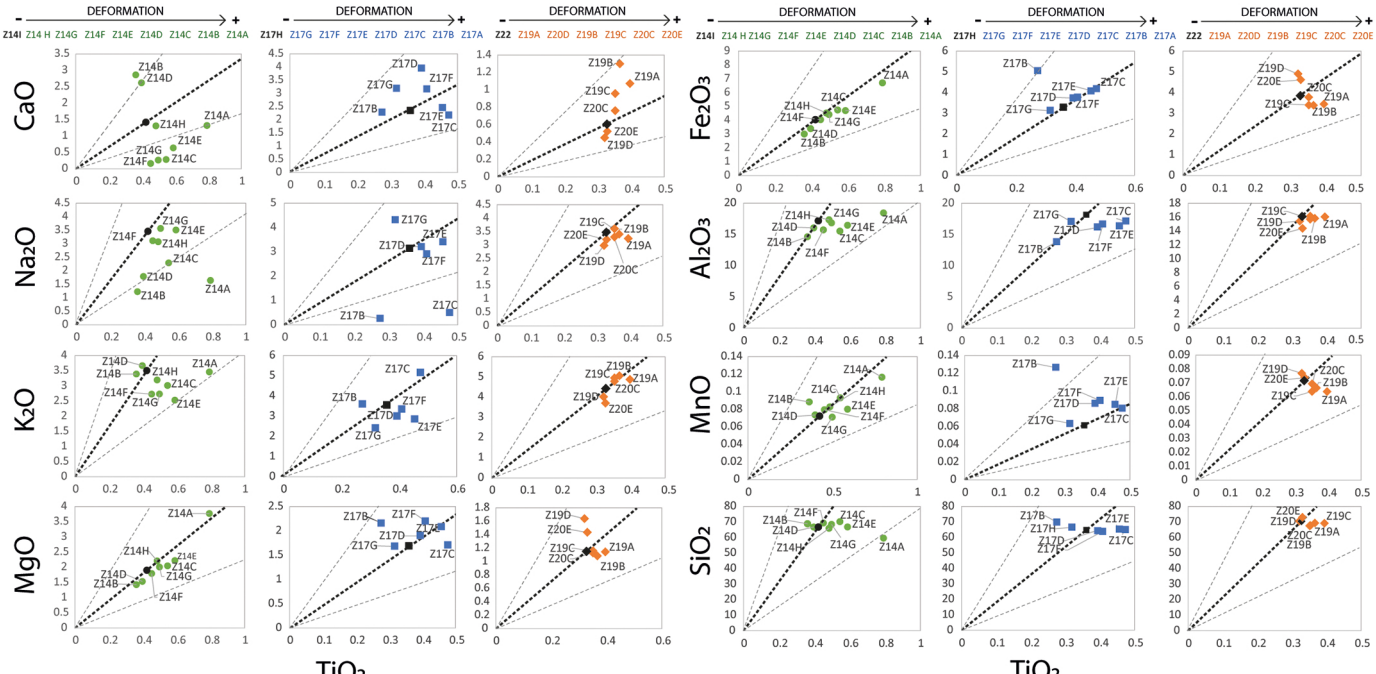
Bielsa B1 transect
Bielsa B2 transect
Maladeta transect
Bielsa B1 transect
Bielsa B2 transect
Maladeta transect
DEFORMATION
CaO
Na2O
K2O
MgO
Fe2O3
Al2O3
MnO
SiO2
TiO2
TiO2

Figure 12

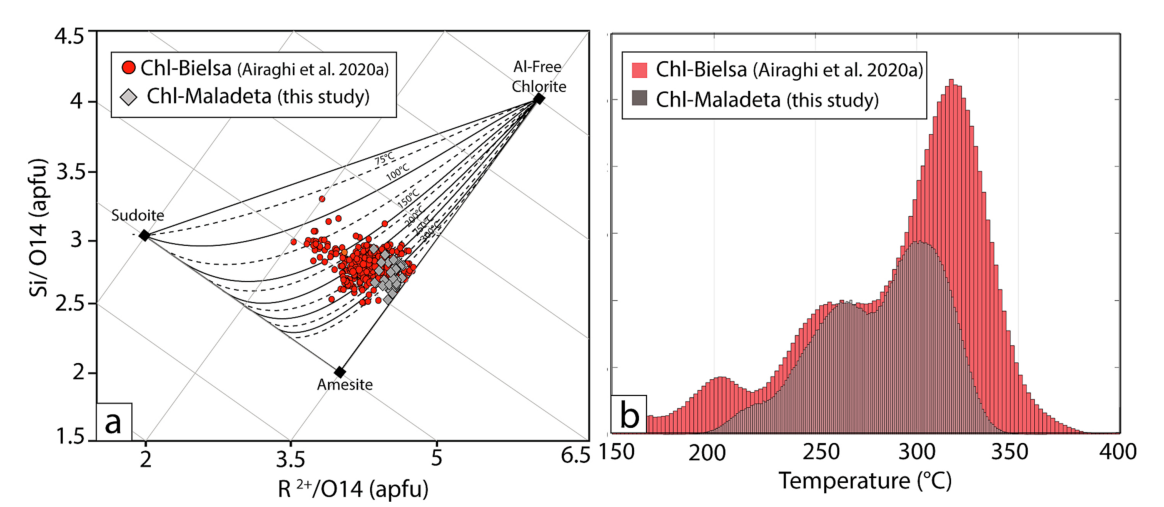
Chl-Bielsa (Airaghi et al. 2020a)
Chl-Maladeta (this study)
Al-Free Chlorite
Sudoite
Amesite
75°C
100°C
150°C
200°C
250°C
300°C
Si/ O14 (apfu)
R 2+/O14 (apfu)
a
b
Temperature (°C)

Figure 13